COMMUNICATION

A small-sized benzothiazole-indolium fluorescent probe: The study of interaction specificity targeting c-MYC promoter G-quadruplex structures and live cell imaging

Received 00th January 20xx,
Accepted 00th January 20xx

DOI: 10.1039/x0xx00000x

Bo-Xin Zheng [a], Meng-Ting She [a], Wei Long [a], Yong-Yu Xu [a], Yi-Han Zhang [a], Xuan-He Huang [a], Wenjie Liu [c], Jin-Qiang Hou [c], Wing-Leung Wong [b,d,*] and Yu-Jing Lu [a,*]

A small-sized c-MYC promoter G-quadruplex selective fluorescent BZT-Indolium binding ligand was demonstrated for the first time as a highly target-specific and photostable probe for *in vitro* staining and live cell imaging and was found able to inhibit the amplification of the c-MYC G-rich sequence (G-quadruplex) and down-regulate oncogene c-MYC transcription in human cancer cells (HeLa).

Target-specific fluorescent probes that selectively bind to biologically important macromolecules, such as proteins and nucleic acids with special structures, can offer a powerful molecular tool for real-time study of their subcellular localization and biofunctions with the advanced fluorescent microscopy techniques. The study of structure-function relationship of targeted biomolecules *in vitro* and *in vivo* thus become feasible.[1-4] For example, green fluorescent proteins are widely used in bio-labelling and dynamic cellular imaging.[5] Some target-specific organic fluorescent probes are attractive alternatives to fluorescent proteins because the molecules can be rationally designed to be small-sized and possess unique functionality, good photophysical properties and tunable emissions from visible to near-infrared.[6-7]

For *in vivo* studies in biological systems, the small-sized molecular probes may exhibit distinctive advantages. However, using small-sized probes to achieve high binding specificity is challenging. In recent years, a number of benzothiazole-based cyanines have been reported.[8] A typical example is the thiazole orange dye (a benzothiazole scaffold bridged with 1-methylquinolinium through methylene), which is a well-known nonspecific staining agent for nucleic acids (DNA and RNA).[9]

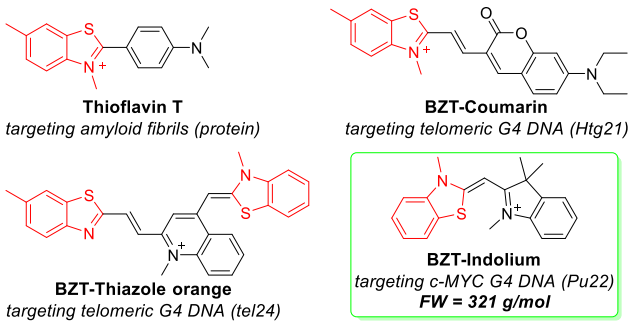

Scheme 1. The benzothiazole-based cyanines as the target-specific fluorescent dyes for protein and G-quadruplex DNA sensing and staining.

Nonetheless, it is quite uncommon that the benzothiazole-based molecular dyes show high recognition specificity towards unique DNA secondary structures such as G-quadruplex (G4) structures over duplex DNA and other nucleic acids. It is noteworthy that when the benzothiazole scaffold is integrated with a unique molecular fragment, its binding specificity towards certain proteins or DNA G4-structures is observed but only few examples have been found in literature thus far. As shown in **Scheme 1**, a small protein sensing probe (**Thioflavin T**) constructed from the benzothiazolium scaffold and dimethylaminobenzene is found selective for amyloid fibrils staining[10] and human telomeric G4-DNA.[11] The benzothiazolium scaffold conjugated via an ethylene bridge with coumarin, **BZT-Coumarin**, becomes a good telomeric G4-DNA probe and is specific to Htg21.[12] Interestingly, as benzothiazolium conjugated with thiazole orange (**BZT-Thiazole orange**), the selectivity is changed to tel24 (a telomeric G4-DNA).[13] These few examples may reveal that the benzothiazole moiety, which has a two-ringed structure with similar size and shape to guanine, could be a useful scaffold for molecular design of G4-specific fluorescent probes for labelling, sensing and imaging of important biomolecules in live cells. We therefore speculated that to integrate an appropriate small-sized group with the benzothiazole scaffold may be able to develop a probe specific to c-MYC promoter G4-DNA, which is recognized as a vital target

[a.] *School of Biomedical and Pharmaceutical Sciences, Guangdong University of Technology, Guangzhou 510006, P. R. China.*
[b.] *State Key Laboratory of Chemical Biology and Drug Discovery, Department of Applied Biology Chemical Technology, The Hong Kong Polytechnic University, Hung Hom, Kowloon, Hong Kong, China..*
[c.] *Department of Chemistry, Lakehead University and Thunder Bay Regional Health Research Institute, 980 Oliver Road, Thunder Bay, On, P7B 6V4, Canada.*
[d.] *School of Biotechnology and Health Sciences, Wuyi University, Jiangmen, 529020, P.R. China.*

Electronic Supplementary Information (ESI) available: Materials, experimental methods and supplementary figures and tables. See DOI: 10.1039/x0xx00000x

for anticancer drug development because the over-expression of c-MYC gene is associated with many cancers.[14-16] However, to discriminate c-MYC promoter G4-DNA from telomere, duplex and single-stranded DNA, and RNA with small-sized probes is challenging.[17-20] To the best of our knowledge, no benzothiazole-based probe specific to c-MYC G4-DNA has been reported to date. We thus developed a small-sized, rigid, and target-specific probe (**BZT-Indolium**) for fluorescent discrimination and imaging of c-MYC promoter G4-DNA *in vitro* and in live cells to reveal their existence. In addition, the ability of the probe on down-regulation of oncogene c-MYC transcription in human cancer cells was investigated.

The photophysical property of **BZT-Indolium** in different solvent systems was investigated (**Figure S1**). The probe in its free rotation form showed only weak emission signal but when it was in the viscous medium (glycerol) its emission signal (F/F_0) was enhanced 75 folds, indicating that the probe is sensitive to the rigidity of the environment that suppresses the intramolecular rotation. This feature of the probe can benefit fluorescent recognition of biomolecules upon interaction *in vitro* and *in vivo*. To discriminate G-quadruplex structures such as c-MYC promoter G4-DNA from other nucleic acids including double-stranded DNA, telomere G4 and RNA in live cells is important and is also a challenging task using small-sized fluorescent probes. As shown in **Figure 1A**, the probe showed very low background fluorescence and the signal intensity was increased significantly upon binding to certain nucleic acids. It is noteworthy that the interaction induced signal (F/F_0) of the probe towards double-stranded DNA (dsDNA) was 1.3-4.1 folds, single-stranded DNA (ssDNA) was 6.6-8.3 folds, RNA was about 2.8 folds, telomere G4-DNA was about 10-19 folds, which are generally lower than the that induced by c-MYC promoter G4-DNA (27-90 folds). In particular, four promoter G4-DNA substrates including pu18 (90-fold), pu22 (86-fold), pu24 (75-fold) and pu27 (73-fold) exhibited extremely strong interaction signal with the probe in solution. These results may suggest that **BZT-Indolium** has high specificity to c-MYC promoter G4-DNA. The equilibrium binding constants (K_{eq}) were estimated (**Table S2**) and were found in good agreement with the induced interaction signals generally. G4-DNA pu18 showed the largest affinity (K_{eq} = 40.5x10^5 M^{-1}) while the binding constants of ssDNA, dsDNA and RNA were weak and less than 3.5x10^5 M^{-1}. The affinity difference is in an order of magnitude. In addition, Job plot analysis showed a 2:1 binding stoichiometry for **BZT-Indolium**-G4-DNA complex formed in solution (**Figure S2 B**).

To further demonstrate the binding specificity of the probe towards c-MYC promoter G4-DNA, *in vitro* competition studies were conducted (**Figure S3-S4**). Using 20 equivalents of RNA or DNA or telo21 G4-DNA can only cause a slight signal reduction for the complex of pu27-**BZT-Indolium**, which may indicate that the probe has much stronger binding affinity and specificity towards pu27 G4-structure. We want to emphasize that **BZT-Indolium** cannot induce G4-structure formation *in vitro*. It also causes no conformational change on the G4-structure as indicated from the interaction with pu27 showing a typical parallel structure in the CD spectra (**Figure S5-S6**: a positive peak at 262 nm and a negative peak at 240 nm). The probe is therefore able to reveal sensitively and selectively the formation of c-MYC promoter G4-DNA structures *in vitro* and in cellular (**Figure S7**). The linear relationship and limit of detection (LOD) were estimated (**Table S3**). It was found that the sensor has a very low LOD (1.27-2.53 nM) towards the c-MYC G4-DNA. Furthermore, the sensing signal of the probe targeting c-MYC G4-DNA, both in solution and PAGE staining (**Figure 1B** and **Figure S10**), is visualizable by naked-eye at low concentration conditions under UV illumination. The probe also exhibited excellent photostability, as demonstrated in **Figure S11**, a steady signal was maintained continuously for 1 h (at 0.5 μM, λ_{ex} = 434 nm, λ_{em} = 477 nm). The probe may be excellent for live cell imaging and *in vivo* studies at low concentration conditions.

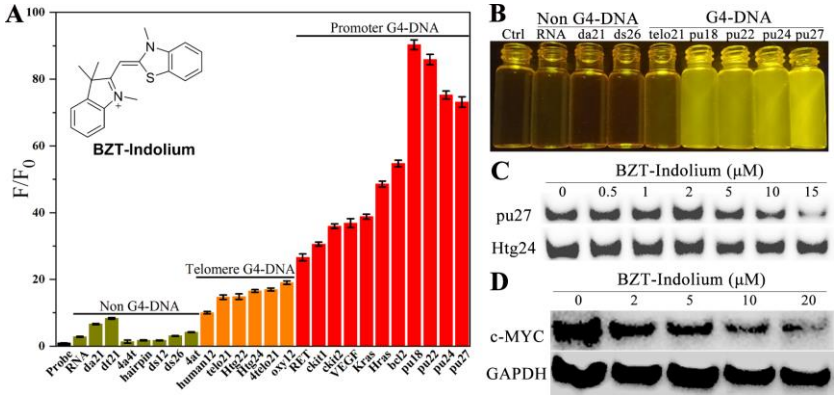

Figure 1. (A) The fluorescence intensity of **BZT-Indolium** in sensing with 25 different nucleic acids. (B) Naked-eye observable fluorescent signal under UV illumination at 302 nm (0.5 μM probe and 2 μM nucleic acids incubated for 10 min). (C) PCR stop assay to compare the effect of the probe to stabilize G4-strutures on Taq DNA polymerase during DNA amplification of oligo sequence of c-MYC promoter G4-DNA (pu27) and telomere G4-DNA (Htg24). (D) qRT-PCR assays to determine the c-MYC mRNA and GAPDH mRNA expression levels in HeLa cells treated with **BZT-Indolium** for 2 days.

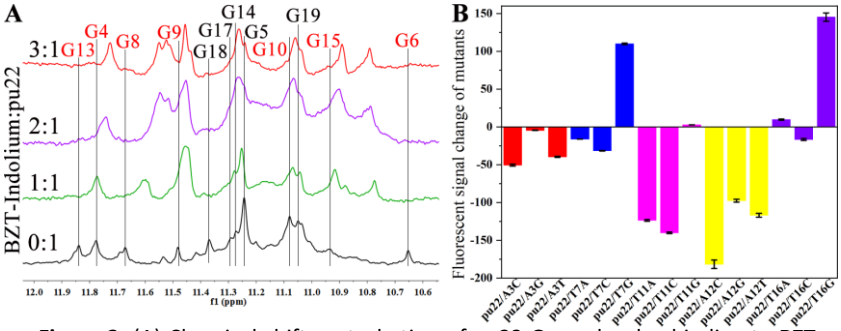

Figure 2. (A) Chemical shift perturbation of pu22 G-quadruplex binding to **BZT-Indolium**. Assays were performed in 25 mM KH_2PO_4 buffer (70 mM KCl, 10% D_2O, pH 7.4) at 25 °C. The final concentration of G4-DNA was 300 μM; (B) Fluorescence binding assays of **BZT-Indolium** with pu22 mutants in Tris-HCl buffer containing 60 mM KCl. Fluorescence signal change = F_{pu22} mutant - F_{pu22} wild type.

The ability of the probe to stabilize c-MYC G4-structures was also evaluated with melting point measurements. The ΔT_m observed for the complex of **BZT-Indolium** with pu18, pu22, pu24 and pu27 in a buffer with 60 mM KCl was about 5.0–5.5 °C while double-stranded DNA (ds26) and telomere G4-DNA (telo21 and Htg24) showed no significant increase (**Figure S13-S14**). The results may support that the probe stabilizes the G4-structures *in vitro*. To further validate the stabilization effect of the probe towards the G4-structure, PCR stop assays were conducted to compare the inhibition effects targeting c-MYC promoter G4-DNA (pu27) and telomere G4-DNA (Htg24) on Taq polymerase during DNA amplification (**Figure 1 C**). For pu27, the PCR products was found decreased gradually upon the addition of the probe and was almost completely disappeared at 15 μM, indicating the probe may stabilize c-MYC G4-DNA and followed inhibits Taq polymerase activity to amplify the DNA. The PCR inhibition caused by the probe was found in a concentration dependent manner and it also affects the expression of c-MYC gene in HeLa cells (**Figure 1 D**). For telomere G4-DNA (Htg24), the inhibition of Taq polymerase activity by the probe is obviously less effective, probably due to its low binding affinity and low stabilization ability towards the telomeric G4-DNA.

The interaction modes of the probe with pu22 G-quadruplex in solution was investigated with ^{1}H NMR (**Figure 2 A**). From the titrations, some imino protons of pu22 was remarkably shifted upon the addition of the probe. At 1:1 molar ratio, the bases of G13, G8, G9, G10, G15 and G6 were strongly influenced, which suggest that interactions may occur at 3' end with T11-A12 loop. As further increasing the probe concentration to the ratio of 2:1 and 3:1, the imino proton of base G4 was significantly shifted, which may imply that the second interaction site is probably at the 5' end with T7 loop. To obtain further information for the interaction sites, fluorescence binding assays of the probe with fifteen pu22 mutants were conducted (**Figure 2 B**). Obviously, the sites at the loops including T7, T11, A12 and T16 showed significant interaction signal influence. This may suggest that the probe is most likely interacting with the loops at these sites and the finding is in accord with the NMR titration results. Molecular docking studies were also conducted and consistent results for the interactions were observed (**Figure S16**).

Real-time visualization and tracking G4-structures in live cells with advanced fluorescence microscopy techniques is important to study their fundamental property and the associated functions. However, it requires target-specific and photostable fluorescent probes that can offer low working concentration. For this purpose, small-sized organic probes may show advantages because they may cause less interference to the biofunction of the binding target; however, to achieve high recognition specificity is challenging with small-sized probes. Our *in vitro* results reveal that **BZT-Indolium** can discriminate c-MYC promoter G4-DNA (pu18, pu22, pu24 and pu27) against non-G4 DNA and telomeric G4-DNA. In addition, the probe cannot induce G4-structure formation. We therefore studied its imaging performance to visualize c-MYC promoter G4-DNA in live cancer cells. **Figure 3 A** showed the imaging of human glioma cells (U87), in which the blue foci were observed in the nuclei and it is particularly obvious in the nucleolus region. The

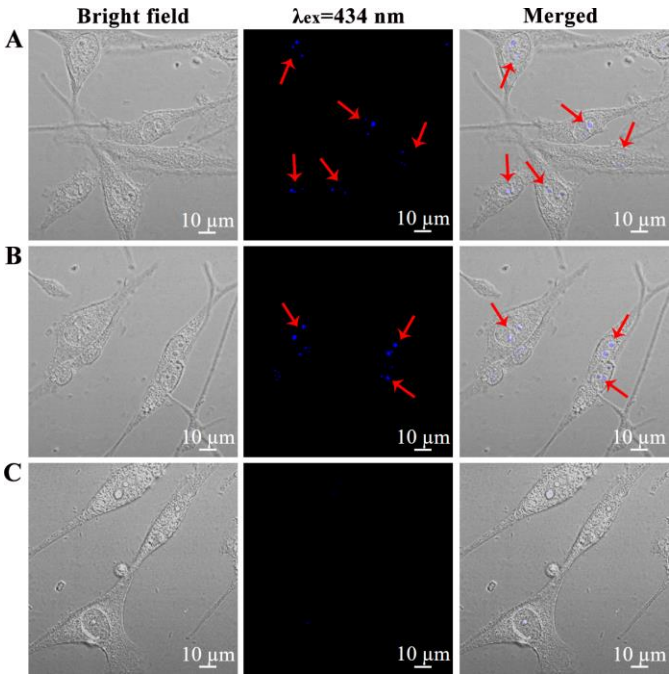

Figure 3. Images of live U87 cells stained with 5 μM **BZT-Indolium**: (A) incubated for 15 min; (B) Treated with RNase for 2 h; (C) Treated with DNase for 2 h.

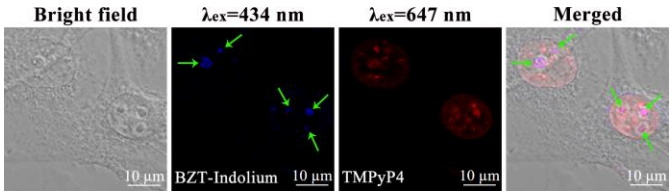

Figure 4. Images of live U87 cells stained with 5 μM **BZT-Indolium** and 5 μM TMPyP4, incubated for 15 min.

observation is consistent with the literature findings that the G-rich sequences are mainly located in the nucleus and nucleolus.[21-22] Similar cellular regions imaged with the probe were also observed in human breast cancer cells (MCF7) and 16HBE (normal cells human bronchial epithelioid cells) shown in **Figure S17-S18**. To confirm the probe binds to DNA but not RNA in cells, enzymatic hydrolysis assays with RNase and DNase were conducted (**Figure 3 B-C**). As expected, the fluorescence foci in the nucleolar region of U87 cells was retained after RNase digestion while the foci were disappeared after DNase assays. To further validate the probe binds to G4-structures in cells as it does *in vitro*, intracellular colocalization experiments with TMPyP4 (a G4-binding ligand) was conducted.[23] From **Figure 4**, the probe stained mainly the nucleolus (blue foci) of U87 cells while TMPyP4 stained a bigger nuclear area. The merged images showed that the staining position of **BZT-Indolium** and TMPyP4 are well colocalized in the nucleolar region. The results may suggest that the probe is able to recognize cellular G4-structures, which is presumably the c-MYC promoter G4-DNA. The intracellular competition experiments with a G4-specific binding ligand, BRACO19, was also conducted in U87 cells.[24] When compared the images in **Figure 5 A** with **B** and **C**, the blue foci of **BZT-Indolium** in the nucleolus region was diminished remarkably after treated with BRACO19, which may indicate

that the probe and BRACO19 compete the same binding target. Moreover, the *in vitro* competition titrations demonstrated that the probe bound to pu27 G4-DNA was substituted by BRACO19 (**Figure S19**) and thus it caused a significant fluorescence signal reduction. These results may further support that the probe binds to G4-DNA in live cells.

Cytotoxicity of **BZT-Indolium** against a number of cell lines including cancer cells U87, HeLa, MCF7 and normal cells 16HBE and HK2 were evaluated with MTT assays (**Figure S20**). From the IC_{50} values (**Table S5**), the probe showed higher toxicity against cancer cells U87, HeLa and MCF7 than the normal cells 16HBE and HK2. The result is reasonable because c-MYC gene is generally overexpressed in many cancer cells and thus the probe may inhibit the expression of c-MYC gene in cells via the stabilization of G4-structures.[14-16] In addition, the less toxicity of the probe against normal cells is an advantage for bio-application in live cell experiments, particularly for those require long-time video tracking of the bio-function and/or dynamics of c-MYC promoter G4-DNA in live cells. More importantly, **BZT-Indolium** bearing a small-sized and simple molecular scaffold may give meaningful insights for the design of cancer drugs targeting G4-structures of c-MYC oncogenes.

In conclusion, a small-sized G4-fluorescent probe was demonstrated to be target-specific towards c-MYC promoter G4-DNA with high photostability. The NMR titration and G4-sequence mutation study showed that the probe may probably interact with the loops of the G4-structure. The intracellular competition and colocalization experiments in live cells showed that the binding target of the probe in live cells presumably is a G4-structure. The probe was found able to reveal the c-MYC G4-DNA formation in live cells, stabilize the structures, inhibit the amplification of the G4-sequence and down-regulate oncogene c-MYC transcription human cancer cells.

This work was supported by the National Nature Science Foundation of China (81473082, 22077020), Nature Science Foundation of Guangdong Province, China (No.: 2017A030313078; 2017A030313071; 2019A1515011799), the Department of Agriculture and Rural Affairs of Guangdong Province, China (2018LM2175), and Jiangmen Program for Innovative Research Team (No. 2018630100180019806).

Conflicts of interest

There are no conflicts to declare.

Notes and references

1 M. D. Antonio, A. Ponjavic, A. Radzevičius, R. T. Ranasinghe, M. Catalano, X. Zhang, J. Shen, L. M. Needham, S. F. Lee, D. Klenerman and S. Balasubramanian, *Nat. Chem.* , 2020, **12**, 832.
2 S. G. Zhang, H. X. Sun, L. X. Wang, Y. Liu, H. B. Chen, Q. Li, A. J. Guan, M. R. Liu and Y. L. Tang, *Nucleic Acids Res.*, 2018, **46**, 7522.
3 M. I. Umar, D Ji, C Y Chan, and C. K. Kwok, *Molecules*, 2019, **24**, 2416.
4 D. Monchaud, *Annu. Rep. Med. Chem.*, 2020, **54**, 133.
5 M. Chalfie, Y. Tu, G. Euskirchen, W. W. Ward and D. C. Prasher, *Science*, 1994, **263**, 802.
6 H. M. Kim and B. R. Cho, *Chem. Rev.*, 2015, **115**, 5014.

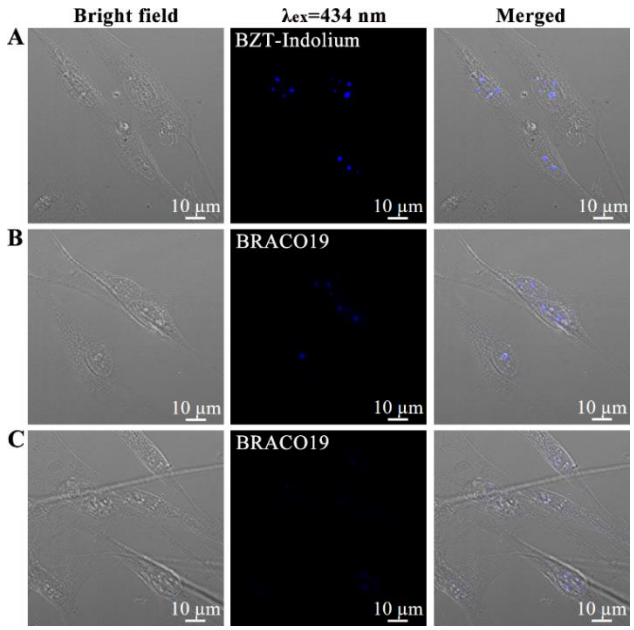

Figure 5. Intracellular competition experiments in live U87 cells and images were taken after incubated for 15 min: (A) 5 μM probe; (B) 5 μM probe and then 5 μM BRACO19; (C) 5 μM probe and then 10 μM BRACO19.

7 J. Yin, Y. Ma, G. Li, M. Peng and W. Lin, *Coordin. Chem. Rev.*, 2020, **412**, 213257.
8 Y. V. Suseela, N. Narayanaswamy, S. Partihar and T. Govindaraju, *Chem. Soc. Rev.*, 2018, **47**, 1098.
9 J. Nygren, N. Svanvik and M. Kubista, *Biopolymers*, 2015, **46**, 39.
10 R. Khurana, C. Coleman, C. Ionescu-Zanetti, S. A. Carter, V. Krishna, R. K. Grover, R. Roy and S. Singh, *J. Struct. Biol.*, 2005, **151**, 229.
11 J. Mohanty, N. Barooah, V. Dhamodharan, S. Hairkrishna, P. I. Pradeepkumar and A. C. Bhasikuttan, *J. Am. Chem. Soc.* ,2013, **135**, 367.
12 J. Yan, Y. Tian, J. Tan and Z. Huang, *Analyst*, 2015, **140**, 7146.
13 Y. Q. Wang, M. H. Hu, R. J. Guo, S. B. Chen, Z. S. Huang and J. H. Tan, *Sensor. Actuat. B-Chem.*, 2018, **266**, 187.
14 C. V. Dang, *Cell*, 2012, **149**, 22.
15 B. J. Chen, Y. L. Wu, Y. Tanaka and W. Zhang, Int. *J. Biol. Sci.*, 2014, **10** 1084.
16 J. Rodríguez, J. Mosquera, J. R. Couceiro, M. E. Vázquez and J. L. Mascareñas, *Angew. Chem. Int. Edit.*, 2016, **55**, 15615.
17 Q. Zhai, C. Gao, J. Ding, Y. Zhang, B. Islam, W. Lan, H. Hou, H. Deng, J. Li, Z. Hu, H. I. Mohamed, S. Xu, C. Cao, S. M. Haider and D. Wei, *Nucleic Acids Res.*, 2019, **47**, 2190.
18 D. Panda, M. Debnath, S. Mandal, I. Bessi, H. Schwalbe and J. Dash, *Sci. Rep.*, 2015, **5**, 13183.
19 M. H. Hu, J. W. Zhou, W. H. Luo, S. B. Chen, Z. S. Huang, R. Wu and J. H. Tan, *Anal. Chem.,* 2019, **91**, 2480.
20 A. Minard, D. Morgan, F. Raguseo, A. D. Porzio, D. Liano, A. G. Jamieson and M. D. Antonio, *Chem. Commun.*, 2020, **56**, 8940.
21 A. Henderson, Y. Wu, Y. C. Huang, E. A. Chavez, J. Platt, F. B. Johnson, R. M. Brosh, Jr, D. Sen and P. M. Lansdorp, *Nucleic Acids Res.*, 2014, **42**, 860.
22 G. Biffi, D. Tannahill, J. Mccafferty and S. Balasubramanian, *Nat. Chem.*, 2013, **5**, 182.
23 A. Siddiqui, C. L. Grand, D. J. Bearss and L. H. Hurley, *P. Natl. Acad. Sci. U. S. A.,* 2002, **99**, 11593.
24 J. Debray, W. Zeghida, M. Jourdan, D. Monchaud, M. L. Dheu-Andries, P. Dumy, M. P. Teulade-Fichou and M. Demeunynck, *Org. Biomol. Chem.*, 2009, **7**, 5219.

Supplementary Information

A small-sized benzothiazole-indolium fluorescent probe: The study of interaction specificity targeting c-MYC promoter G-quadruplex structures and live cell imaging

Bo-Xin Zheng [a], Meng-Ting She [a], Wei Long [a], Yong-Yu Xu [a], Yi-Han Zhang [a], Xuan-He Huang [a], Wenjie Liu [c], Jin-Qiang Hou [c], Wing-Leung Wong [b,d,*] and Yu-Jing Lu [a,*]

[a] School of Biomedical and Pharmaceutical Sciences, Guangdong University of Technology, Guangzhou 510006, P. R. China.

[b] State Key Laboratory of Chemical Biology and Drug Discovery, Department of Applied Biology Chemical Technology, The Hong Kong Polytechnic University, Hung Hom, Kowloon, Hong Kong, China.

[c] Department of Chemistry, Lakehead University and Thunder Bay Regional Health Research Institute, 980 Oliver Road, Thunder Bay, On, P7B 6V4, Canada.

[d] School of Biotechnology and Health Sciences, Wuyi University, Jiangmen, 529020, P.R. China.

* Corresponding Author

W.-L. Wong: wing.leung.wong@polyu.edu.hk.

Y.-J. Lu: luyj@gdut.edu.cn.

List of contents

added subsequently, the concentration ratio is 10/1. (B) CD spectra of pu27 (5 μM) interacted with the probe without K^+ ion and with 60 mM KCl in 10 mM Tris-HCl buffer at pH 7.4.

Figure S6. CD spectra of c-MYC G4-DNA (5 μM) interacted with different concentration of **BZT-Indolium** (1 to 3 equivalents) in 10 mM Tris-HCl buffer with 60 mM KCl at pH 7.4: (A) pu18; (B) pu22; (C) pu24; and (D) pu27.

Figure S7. (A) Linear relationship of probe **BZT-Indolium** in the detection of pu18; (B) Linear relationship of probe **BZT-Indolium** in the detection of pu22; (C) Linear relationship of probe **BZT-Indolium** in the detection of pu24; (D) Linear relationship of probe **BZT-Indolium** in the detection of pu27. The concentration of **BZT-Indolium** was 0.5 μM in Tris−HCl buffer (10 mM, pH 7.4) containing 60 mM KCl.

Figure S8. UV-vis titration spectra of **BZT-Indolium** (10 μM) with different concentration of c-MYC G4-DNA in a Tris-HCl buffer (10 mM, pH = 7.4) containing 60 mM KCl: (A) pu18; (B) pu22; (C) pu24; and (D) pu27.

Figure S9. (A) The linear fitting of the absorption intensity by the fluorescence emission spectral integral area of **BZT-Indolium** in pu18; (B) The linear fitting of the absorption intensity by the fluorescence emission spectral integral area of **BZT-Indolium** in pu22; (C) The linear fitting of the absorption intensity by the fluorescence emission spectral integral area of **BZT-Indolium** in pu24; (D) The linear fitting of the absorption intensity by the fluorescence emission spectral integral area of **BZT-Indolium** in pu27. The concentration of **BZT-Indolium** was 0.5 μM in Tris−HCl buffer (10 mM, pH 7.4) containing 60 mM KCl.

Figure S10. (A) Gel electrophoresis (20 % acrylamide in 1 × TBE) of da21, ds26, 4at, telo21, pu18, pu22, pu24, pu27 at a concentration of 5.0 μM and was stained with **BZT-Indolium** (5.0 μM) for 15 min; (B) Gel electrophoresis (20 % acrylamide in 1 × TBE) of da21, ds26, 4at, telo21, pu18, pu22, pu24, pu27 at a concentration of 5.0 μM and was stained with **SYBR Gold** (5.0 μM) for 15 min.

Figure S11. The curve of fluorescence intensity with time (1 h) after the combination of probe **BZT-Indolium** (0.5 μM) with c-MYC promoter G4-DNA (pu18, pu22, pu24, pu27) (1.0 μM). The excitation wavelength λ_{ex} = 434 nm, the emission wavelength λ_{em} = 477 nm.

Figure S12. Fluorescence decay traces of **BZT-Indolium** (0.5 μM, λ_{ex} = 320 nm, λ_{em} = 477 nm) in the absence and in the presence of different DNA substrates including ds26, telo21, pu18, pu22, pu24 and pu27 in 10 mM Tris-HCl buffer at pH 7.4 containing 60 mM KCl.

Figure S13. The evaluation the G4-structure stabilization ability of **BZT-Indolium** in 10 mM Tris-HCl buffer at pH 7.4 containing 60 mM KCl: (A) Normalized CD signal of pu18 during melting process; (B) Normalized CD signal of pu22 during melting process; (C) Normalized CD signal of pu24 during melting process; (D) Normalized CD signal of pu27 during melting process. The G-quadruplex was characterized by the positive peak at 262 nm.

Figure S14. The evaluation the stabilization ability of **BZT-Indolium** in 10 mM Tris-HCl buffer at pH 7.4 containing 60 mM KCl: (A) Normalized CD signal of double stranded DNA (ds26) during melting process, the double stranded DNA was characterized by the negative peak at 242 nm; (B) Normalized CD signal of Telomere G4-DNA (telo21) during melting process, the G-quadruplex was characterized by the positive

peak at 290 nm; (C) Normalized CD signal of Telomere G4-DNA (Htg24) during melting process, the G-quadruplex was characterized by the positive peak at 290 nm.

Figure S15. Expression rate of c-MYC mRNA at different concentrations of **BZT-Indolium**.

Figure S16. The molecular docking study of **BZT-Indolium** in complex with pu22 G-quadruplex.

Figure S17. (A) Fluorescence images of live MCF-7 cells stained with 5.0 μM **BZT-Indolium** for 15 min; (B) Fluorescence images of live MCF-7 cells stained with 5.0 μM **BZT-Indolium** for 15 min and RNase treated for 2 h; (C) Fluorescence images of live MCF-7 cells stained with 5 μM **BZT-Indolium** for 15 min and DNase treated for 2 h.

Figure S18. Fluorescence images of live normal cells 16HBE stained with 5.0 μM **BZT-Indolium** for 15 min.

Figure S19. Fluorescence response of **BZT-Indolium** (0.5 μM) added to pu27 G4-DNA and BRACO19 was added subsequently. The concentration ratio between **BZT-Indolium** and BRACO19 is 1: 1 and 1: 2.

Figure S20. (A) Cells survival viability of U87 cells; (B) Cells survival viability of HeLa cells; (C) Cells survival viability of MCF7 cells; (D) Cells survival viability of 16HBE cells; (E) Cells survival viability of HK2 cells. The concentration gradients of **BZT-Indolium** were 0, 0.3125, 0.625, 1.25, 5, 10 and 20 μM.

Figure S21. Fluorescence titration spectra of **BZT-Indolium** with different nucleic acids: RNA; single-stranded DNA: da21, dt21; duplex DNA: 4a4t, hairpin, ds12, ds26, 4at; Telomere G4-DNA: human12, telo21, Htg22, Htg24, 4telo21, oxy12; Promoter G4-DNA: RET, ckit1, ckit2, VEGF, Kras, Hras, bcl2, pu18, pu22, pu24 and pu27 in a Tris-HCl buffer (10 mM, pH 7.4) containing 60 mM KCl. Fluorescence signal was measured at 25 °C.

Figure S22. Fluorescence titrations, presented as a relative increase of the integral fluorescence (F/F_0) of different nucleic acids: RNA; single-stranded DNA: da21, dt21; duplex DNA: 4a4t, hairpin, ds12, ds26, 4at; Telomere G4-DNA: human12, telo21, Htg22, Htg24, 4telo21, oxy12; Promoter G4-DNA: RET, ckit1, ckit2, VEGF, Kras, Hras, bcl2, pu18, pu22, pu24 and pu27 with **BZT-Indolium** (0.5 μM) in 10 mM Tris-HCl buffer (pH 7.4, containing 60 mM KCl).

Figure S23. (A) The UV absorption spectrum obtained by adding five continuous concentrations (0.4 μM, 0.8 μM, 1.2 μM, 1.6 μM ,2.0 μM) of **BZT-Indolium** to a fixed concentration of 1 μM pu18; (B) The UV absorption spectrum obtained by adding five continuous concentrations (0.4 μM, 0.8 μM, 1.2 μM, 1.6 μM ,2.0 μM) of **BZT-Indolium** to a fixed concentration of 1 μM pu22; (C) The UV absorption spectrum obtained by adding five continuous concentrations (0.4 μM, 0.8 μM, 1.2 μM, 1.6 μM, 2.0 μM) of **BZT-Indolium** to a fixed concentration of 1 μM pu24; (D) The UV absorption spectrum obtained by adding five continuous concentrations (0.4 μM, 0.8 μM, 1.2 μM, 1.6 μM, 2.0 μM) of **BZT-Indolium** to a fixed concentration of 1 μM pu27.

Figure S24. (A) Fluorescence spectrum obtained by adding five continuous concentrations of **BZT-Indolium** (0.4 μM, 0.8 μM, 1.2 μM, 1.6 μM, 2.0 μM) to a fixed concentration of 1 μM pu18; (B) Fluorescence spectrum obtained by adding five continuous concentrations of **BZT-Indolium** (0.4 μM, 0.8 μM, 1.2 μM, 1.6 μM, 2.0 μM) to a fixed concentration of 1 μM pu22; (C) Fluorescence spectrum obtained

by adding five continuous concentrations of **BZT-Indolium** (0.4 μM, 0.8 μM, 1.2 μM, 1.6 μM, 2.0 μM) to a fixed concentration of 1 μM pu24; (D) Fluorescence spectrum obtained by adding five continuous concentrations (0.4 μM, 0.8 μM, 1.2 μM, 1.6 μM, 2.0 μM) of **BZT-Indolium** to a fixed concentration of 1 μM pu27.

Figure S25. UV-vis titration spectra of **BZT-Indolium** (10 μM) with selected nucleic acids in a Tris-HCl buffer (10 mM, pH = 7.4) with 60 mM KCl at 25 °C: (A) RNA. (B) dt21. (C) ds26. (D) telo21 G4-DNA.

Figure S26. Fluorescence titration spectra of **BZT-Indolium** with different concentrations of pu22 mutants. The concentration of **BZT-Indolium** was 0.5 μM in Tris−HCl buffer (10 mM, pH 7.4) containing 60 mM KCl.

Figure S27. CD spectra of 5 μM pu22/A3C, pu18/A3G, pu22/A3T, pu22/T7A, pu22/T7C, pu22/T7G, pu22/T11A, pu22/T11C, pu22/T11G, pu22/A12C, pu22/A12G, pu22/A12T, pu22/T16A, pu22/T16C, pu22/T16G binding to **BZT-Indolium** in 10 mM Tris-HCl buffer at pH 7.4 with 60 mM KCl.

Figure S28. ^{1}H NMR (DMSO-d_6), HRMS of intermediate **A**.

Figure S29. ^{1}H NMR (DMSO-d_6), HRMS of intermediate **B**.

Figure S30. ^{1}H NMR (DMSO-d_6), ^{13}C NMR (DMSO-d_6), HRMS of **BZT-Indolium**.

Section A: Experimental

1. Materials

All the reagents and chemicals are AR grade and need no further purification. All the oligonucleotides were synthesized and purified by Thermo Fisher Scientific and their sequences were listed in **Table S1**. Besides, ^{1}H and ^{13}C NMR spectra were recorded at 400 MHz and 100 MHz in DMSO-d_6 with a Bruker BioSpin GmbH spectrometer. High resolution mass spectra (HRMS) were obtained by Agilent 1260-6230 TOF. The cell lines used in this study including U87 cells (human glioma cells, ATCC® HTB-14™), HeLa cells (Human cervical cancer cells, ATCC® CRM-CCL-2™), MCF7 cells (human breast cancer cells, ATCC® HTB-22™), 16HBE cells (human bronchial epithelioid cells, ATCC® CRL-4051™), and HK2 (human renal tubular epithelial cells, ATCC® CRL-2190™) were purchased from ATCC.

2. The synthesis and characterization of BZT-Indolium:

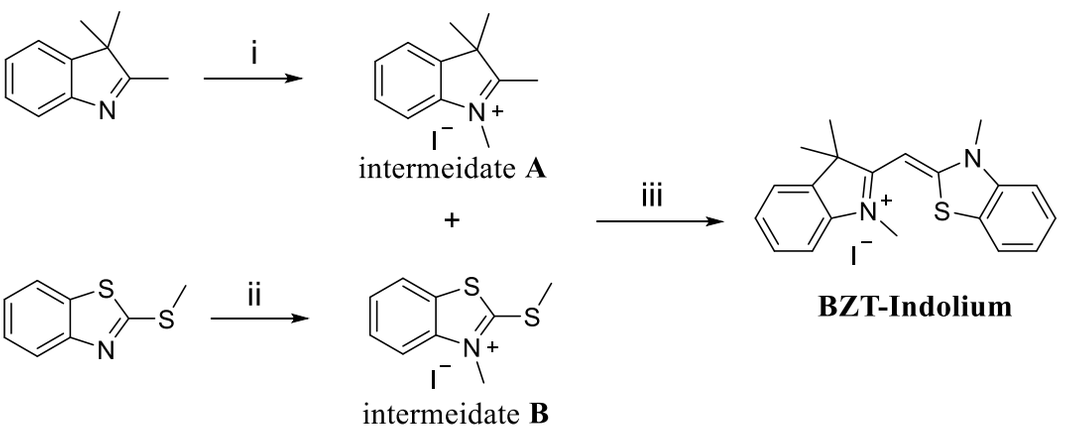

Scheme S1. Synthesis route to **BZT-Indolium** and its molecular structures. Reagents and conditions: (i) iodomethane, acetonitrile, 80 °C, 8 h; (ii) iodomethane, acetonitrile, 80 °C, 8 h; (iii) acetonitrile, triethylamine, 70 °C, 8 h.

2.1 Synthesis of intermediate A: 1,2,3,3-tetramethyl-3H-indol-1-ium

2,3,3-trimethyl-3H-indole (2.0 mmol) and iodomethane (3.0 mmol) was added to a clean round bottom flask and then add 8.0 ml of acetonitrile to dissolve them. The mixture was refluxed at 80 ℃ for 8 h. After the reaction was confirmed by TLC, 15.0 ml ethyl acetate was added to precipitate the solid, and the intermediate **A** was obtained by recrystallization of ethanol. The compounds were characterized with ^{1}H NMR. Pink solid, yield 85.7 %. ^{1}H NMR (400 MHz, DMSO) δ 7.92 (dd, J = 5.7, 3.0 Hz, 1H), 7.85 – 7.81 (m, 1H), 7.63 (dd, J = 6.3, 2.7 Hz, 2H), 3.98 (s, 3H), 2.77 (s, 3H), 1.54 (s, 6H). HRMS m/z: calcd for $C_{12}H_{16}^{+}$, $[M-I]^{+}$ = 174.1279, found 174.1279.

2.2 Synthesis of intermediate B: 3-methyl-2-(methylthio)benzo[d]thiazol-3-ium

2-(methylthio)benzo[d]thiazole (2.0 mmol) and iodomethane (3.0 mmol) was added to a clean round bottom flask and then add 8.0 ml of acetonitrile to dissolve them. The mixture was refluxed at 80 ℃ for 8 h. After the reaction was confirmed by TLC, 15.0 ml ethyl acetate was added to precipitate the solid, and

the intermediate **B** was obtained by recrystallization of ethanol. The compounds were characterized with ^{1}H NMR. White solid, yield 83.4 %. ^{1}H NMR (400 MHz, DMSO) δ 8.41 (dd, *J* = 8.1, 0.6 Hz, 1H), 8.21 (d, *J* = 8.4 Hz, 1H), 7.85 (dd, *J* = 8.5, 7.4, 1.2 Hz, 1H), 7.76 – 7.71 (m, 1H), 4.12 (s, 3H), 3.14 (s, 3H). HRMS m/z: calcd for $C_9H_{10}NS_2^+$, $[M-I]^+$ = 196.0245, found 196.0245.

2.3 Synthesis of BZT-Indolium: (Z)-1,3,3-trimethyl-2-((3-methylbenzo[d]thiazol-2(3H)-ylidene)methyl)-3H-indol-1-ium

The intermediates **A** (1.5 mmol) and **B** (1.5 mmol) was added to a clean round bottom flask and then add 6.0 ml of acetonitrile to dissolve them. In addition, triethylamine (0.5 mmol) was added as catalyst. The mixture was refluxed at 70 ℃ for 8 h. After the reaction was confirmed by TLC, 10.0 ml ethyl acetate was added to precipitate the solid, and the end products **BZT-Indolium** were obtained by recrystallization of ethanol. The compounds were characterized with ^{1}H, ^{13}C NMR, and HRMS. Orange solid, yield 76.6 %. ^{1}H NMR: (400 MHz, DMSO) δ 8.17 (d, *J* = 7.4 Hz, 1H), 7.97 (d, *J* = 8.4 Hz, 1H), 7.71 (m, 1H), 7.57 (m, 2H), 7.41 (m, 2H), 7.26 (t, *J* = 7.3, 1H), 6.08 (s, 1H), 4.05 (s, 3H), 3.60 (s, 3H), 1.69 (s, 6H). ^{13}C NMR (101 MHz, DMSO): δ 174.82, 165.11, 144.01, 141.14, 139.93, 128.92, 126.44, 125.22, 123.70, 122.84, 115.24, 111.57, 82.89, 49.80, 35.52, 25.32. HRMS m/z: calcd for $C_{20}H_{21}N_2S^+$, $[M-I]^+$ = 321.1416, found 321.1416.

3. Methods

3.1 UV-Vis and fluorescence analysis

In this study, the UV-Vis spectrum was obtained by using Lambda 25 Spectrophotometer (Perkin Elmer). The fluorescence spectrum was recorded on the LS-45 fluorescence spectrometer (Perkin Elmer). The slit width of the colorimetric dish is 1 mm and optical diameter is 10 mm.

The calculation of fluorescence quantum yields was based on the equation: $\Phi_x = \Phi_{ST} (Grad_x / Grad_{ST}) (\eta^2_x / \eta^2_{ST})$.[1] In the equation, the subscript ST represents standard, the subscript X represents test, Φ represents fluorescence quantum yields, Grad represents gradient from the plot of integrated fluorescence intensity versus absorbance, and η represents refractive index of the solvent. In the present study, the standard used was fluorescein (1 % NaOH ethanol, Φ = 0.95).[2]

3.2 Fluorescence lifetime study

Fluorescence lifetime decays were recorded using HORIBA Fluorolog. The method is time-correlated single-photon counting (TCSPC). The experiments were performed using 0.5 μM concentration of the **BZT-Indolium** in 10 mM Tris-HCl buffer at pH 7.4 containing 60 mM KCl, λ_{ex} = 320 nm, λ_{em} = 477 nm. The slit is 29 nm.

3.3 The limit of detection (LOD)

The limit of detection (LOD) of the compounds were obtained by fluorescence titration and estimated based on the calculation formula: LOD = K (S_b/m). In the equation, S_b is the standard deviation of the blank multiple measurements (n = 20), and m is the slope of the calibration curve, which represents the sensitivity of this method. In addition, according to the International Union of Pure and Applied Chemistry (IUPAC), K value is generally taken to be 3.

3.4 Circular dichroism (CD) and melting point test

The CD spectra were performed on a Chirascan spectrophotometer (Applied Photophysics). During the experiment, a quartz cuvette with a length of 1 mm was used to record the spectrum in a wavelength range of 220 to 340 nm with a 1 nm bandwidth, a 1 nm step and 0.5 s per point. The melting point test was set at a fixed wavelength, while gradually increasing the temperature from 25 to 95 °C, 1 nm step size, and 5 s per point. The experiments were performed using 8 μM **BZT-Indolium** and 4 μM DNA in 10 mM Tris-HCl buffer at pH 7.4 containing 60 mM KCl.

3.5 Native PAGE experiment conditions

The gel electrophoresis was based on 30 % (29:1) polyacrylamide gels with a size of 160 x 140 x 0.75 mm. The oligonucleotides used in the experiment included various single-, duplex- and quadruplex-forming oligonucleotides, with a fixed concentration of 5 μM, and they were run in 1 x TBE buffer (80 mM Tris-borate, 2 mM EDTA, pH 8.3). The experimental parameters were as follows: temperature = 0 °C, voltage = 110 V, time = 4 h. Finally, the removed gel was stained with compound **BZT-Indolium** (5 μM) in 1 x TBE for 20 min. Meanwhile, a commercial SYBR Gold (5 μM) was used to stain another gel as a control.[3]

3.6 Fluorescence microscopy imaging study and cell staining

Cancer cells human glioma cells (U87), human breast cancer cells (MCF7) and normal cells human bronchial epithelioid cells (16HBE) were cultured in confocal dishes for 24 h. After the removal of medium, the confocal dishes were washed with pre-cooled PBS for three times. After washing, the cells were fixed by pre-cooled 99 % methanol (-4 °C) for 1 min. Then, the sample was washed with pre-cooled PBS for 3 times. **BZT-Indolium** (5 μM) was added and then stained for 15 min. Finally, the confocal dishes were washed with pre-cooled PBS for six times and then it was observed under confocal microscope. The excitation wavelengths was 434 nm for **BZT-Indolium**. The digital images were then recorded on confocal laser scanning microscopy (ZEISS LSM 800 with Airscan).

3.7 DNase and RNase digestion tests

On the basis of fluorescence microscopy imaging study, 1 mL DNase (Sigma, 50 μg/mL) and RNase (GE, 50 μg/mL) were added to the confocal dishes respectively and then the sample was cultured at 37 °C for 2 h under 5 % CO_2. After that, the solution was removed from the confocal dishes and the sample was washed with pre-cooled PBS for 6 times. Finally, the digital images were recorded on confocal laser scanning microscopy (ZEISS LSM 800 with Airscan).

3.8 Confocal imaging of co-localization

Cancer cells human glioma cells (U87) were cultured in confocal dishes for 24 h. After the removal of medium, the confocal dishes were washed with pre-cooled PBS for three times. After washing, the cells were fixed by pre-cooled 99 % methanol (-4 °C) for 1 min. Then, the sample was washed with pre-cooled PBS for 3 times. **BZT-Indolium** (5.0 μM) was added and then stained for 15 min. After that, the sample was washed with pre-cooled PBS for 3 times, and TMPyP4 (5.0 μM) was added and then stained for 15 min. Finally, the confocal dishes were washed with pre-cooled PBS for six times and then it was observed

under confocal microscope. The excitation wavelength of **BZT-Indolium** is set to 434 nm and that of TMPyP4 is set to 647 nm. The digital images were then recorded on confocal laser scanning microscopy (ZEISS LSM 800 with Airscan).

3.9 Cell competitive test

Cancer cells human glioma cells (U87) were cultured in confocal dishes for 24 h. After the removal of medium, the confocal dishes were washed with pre-cooled PBS for three times. After washing, the cells were fixed by pre-cooled 99 % methanol (-4 °C) for 1 min. Then, the sample was washed with pre-cooled PBS for 3 times. **BZT-Indolium** (5.0 μM) was added and then stained for 15 min. After that, the sample was washed with pre-cooled PBS for 3 times, and BRACO19 (5.0 μM and 10.0 μM) was added for 15 min. Finally, the confocal dishes were washed with pre-cooled PBS for six times and then it was observed under confocal microscope. The excitation wavelength of **BZT-Indolium** is set to 434 nm. The digital images were then recorded on confocal laser scanning microscopy (ZEISS LSM 800 with Airscan).

3.10 PCR stop assay

Polymerase stop assay was performed using a modified protocol previous reported.[4] In short, the PCR stop assay was conducted by introducing different concentrations of compound (0–15 μM) into 25 μl solution containing 1X PCR buffer, 2 μM of each oligomer, 0.16 mM dNTP and 2.5 U Taq polymerase (Invitrogen, USA). Reaction mixtures were incubated in a thermocycler under the following cycling conditions: 94 °C for 5 min, 30 cycles of 94 °C for 30 s, 56 °C for 30 s and 72 °C for 30 s. Amplified products were resolved on 20 % polyacrylamide gel and stained with SYBR Gold (Invitrogen, USA).

3.11 RT-PCR

HeLa cells were incubated in 6-well plates with different concentrations of **BZT-Indolium** (0, 2, 5, 10, 20 μM) for 48 hours, then the medium was removed and washed three times with precooled PBS. HeLa cells were dissolved with TRIzol, and the total RNA was extracted according to the manufacturer's instructions. Finally, the extracted RNA was dissolved in distilled deionized water containing 0.1% diethyl pyrocarbonate (DEPC), and the final volume was 50 μL. Each reaction mixture (20 μL) contained 2 × One Step SYBR Green Mix 10 μL, One Step SYBR Green Enzyme Mix 1 μL, 50 × ROX Reference Dye 1 0.4 μL, Gene Specific Primer Forward (10 μM) 0.4 μL, Gene Specific Primer Reverse (10 μM) 0.4 μL, 1 μg of total RNA and RNase-free ddH2O to 20 μL. The reaction mixtures were incubated in a thermocycler under the following cycling conditions: denature at 94 °C for 3 min, followed by 30 cycles at 94 °C for 45 s, 60 °C for 30 s and 72 °C for 45 s, and elongation 72 °C for 10 min. Amplified products were resolved on 20 % polyacrylamide gel and stained with SYBR Gold (Invitrogen, USA). The primers used in the real-time RT-PCR were as follows: c-MYCA, 5′-TGGTGCTCCATGAGGAGACA-3′; c-MYCS, 5′-GTGGCACCTCTTGAGGACCT-3′. GAPDH is used as an internal control for normalization, the internal control GAPDH is amplified by the forward primer 5′-GGGAAACTGTGGCGTGAT-3′ and the reverse primer 5′-GAGTGGGTGTCGCTGTTGA-3′. A comparative Ct (ΔΔCT) method was used to compare the mRNA expression levels of genes of interest.

3.12 MTT assay

Both cancer cells U87 cells, HeLa cells and MCF7 cells and normal cells 16HBE cells and HK2 cells were used in the MTT experiments. The cells were cultured on 96-well plates with a density of 5000 cells per well approximately. The culture medium were DMEM (U87), DMEM (HeLa), DMEM (MCF7), DMEM (16HBE) and HK2 (F12) and the culture condition was set at 37 °C and 0.5 % CO_2. After cultured for 24 h, the 96-well plate was washed three times with pre-cooled PBS and then U87 cells, 16HBE cells and HK2 cells were treated with **BZT-Indolium** solutions at different concentrations (0, 0.3125, 0.625, 1.25, 2.5, 5, 10, and 20 μM) for 48 h, respectively. After culture, the medium was decanted and 5 mg/mL of MTT solution, 200 μL per well, was added to the sample and then incubated for 4 h in dark. Then, the MTT solution was decanted and DMSO (100 μL per well) was added to ensure the deck adhering to 96-well plate complete dissolution. These treated 96-well plates were measured for absorbance with an enzyme label and the absorption wavelength was 577 nm. Finally, the cell survival rate and the half maximal inhibitory concentration (IC_{50}) of compound **BZT-Indolium** on the cells were calculated from the obtained absorbance values.

3.13 Molecular docking study

The solution structure of human c-MYC promoter G4-DNA was used to perform molecular docking studies (PDB ID: 6o2l).[5] The 3D structure of BZT-Indolium ligand were generated using DS viewer 3.5. Molecular docking was performed using AUTODOCK vina program.[6] The dimensions of the grid box were set large enough to encompass the whole G-quadruplex structure. All other parameters were left as default.

Section B: Supporting Tables and Figures

Table S1. Sequences of oligonucleotides used in the present study.

Abbreviation	Source/Sequence (5′→3′)	Structure/origin
RNA	16S- and 23S-Ribosomal from *E. coli*	Duplex
da21	AAAAAAAAAAAAAAAAAAAAA	Single-stranded
dt21	TTTTTTTTTTTTTTTTTTTT	Single-stranded
4a4t	AAAATTTT	Duplex
hairpin	CGCGCGCGTTTTCGCGCGCG	Duplex
ds12	GCGCAATTGCGC	Duplex
ds26	CAATCGGATCGAATTCGATCCGATTG	Duplex
4at	GCGCAATTGCGC	Duplex
human12	TTAGGGTTAGGG	Telomere G-quadruplex
telo21	GGGTTAGGGTTAGGGTTAGGG	Telomere G-quadruplex
Htg22	AGGGTTAGGGTTAGGGTTAGGG	Telomere G-quadruplex
Htg24	TTGGGTTAGGGTTAGGGTTAGGGA	Telomere G-quadruplex
4telo21	GGGTTAGGGTTAGGGTTAGGGTTAGGGTTAG	Telomere G-quadruplex
oxy12	GGGGTTTTGGGG	Telomere G-quadruplex
RET	GGGGCGGGGCGGGGCGGGGG	Promoter G-quadruplex
ckit1	AGGGAGGGCGCTGGGAGGAGGG	Promoter G-quadruplex
ckit2	GGGCGGGCGCGAGGGAGGGG	Promoter G-quadruplex
VEGF	GGGGCGGGCCGGGGGCGGGG	Promoter G-quadruplex
Kras	GGGCGGTGTGGGAAGAGGGAAGAGGGG	Promoter G-quadruplex
Hras	TCGGGTTGCGGGCGCAGGGCACGGGCG	Promoter G-quadruplex
bcl2	GGGCGCGGGAGGAAGGGGGCGGG	Promoter G-quadruplex
pu18	AGGGTGGGGAGGGTGGGG	Promoter G-quadruplex
pu22	TGAGGGTGGGTAGGGTGGGTAA	Promoter G-quadruplex
pu24	TGAGGGTGGGGAGGGTGGGGAAGG	Promoter G-quadruplex
pu27	TGGGGAGGGTGGGGAGGGTGGGGAAGG	Promoter G-quadruplex

Table S2. F/F_0 and binding constants for **BZT-Indolium** with different oligonucleotide determined from the fitted curves (λ_{ex} = 434 nm, λ_{em} = 477 nm).

Oligonucleotides	Binding signal, F/F_0 [a]	Binding constants [b] K_{eq} ($\times 10^5$ M^{-1})
RNA	2.8	n.d.
da21	6.6	2.74±0.18
dt21	8.3	3.48±0.14
4a4t	1.3	n.d.
hairpin	1.7	n.d.
ds12	1.7	n.d.
ds26	3.0	n.d.
4at	4.1	1.95±0.21
human12	10.0	5.06±0.67
telo21	14.7	7.13±1.04
Htg22	14.8	7.42±0.46
Htg24	16.5	7.79±0.38
4telo21	16.9	8.25±0.92
oxy12	19.0	9.63±0.28
RET	26.6	11.18±1.17
ckit1	30.5	14.54±1.33
ckit2	35.9	16.98±0.85
VEGF	36.8	17.28±1.04
Kras	38.8	18.47±1.12
Hras	48.6	24.25±1.98
bcl2	54.7	27.81±1.06
pu18	90.3	40.53±1.57
pu22	85.8	37.74±1.73
pu24	75.3	34.07±1.65
pu27	73.1	33.92±1.29

[a] The concentrations of **BZT-Indolium** and oligonucleotides are 0.5 μM and 9.0 μM.

[b] Equilibrium binding constant of **BZT-Indolium** with oligonucleotides at 25 °C; n.d. denoted as not determined because the ligand-DNA binding signal is too weak for estimation.

Table S3. The spectroscopic data of **BZT-Indolium** with c-MYC G-quadruplex DNA.[a]

	Absorbance (λ_{max}, nm)	λ_{em} (nm)	Stokes shift	Φ_f [b]	Lifetime (ns)	K_{eq} ($\times 10^5$ M^{-1})	LOD [c] (nM)	Lr [e] (μM)	R^2
pu18	434	477, 502	43, 68	0.28±0.022	4.49	40.53±1.57	1.63	0.142-2.84	0.9816
pu22	434	477, 502	43, 68	0.24±0.015	4.07	37.74±1.73	1.27	0.142-2.272	0.9873
pu24	434	477, 502	43, 68	0.23±0.013	4.12	34.07±1.65	2.53	0.284-2.84	0.9803
pu27	434	477, 502	43, 68	0.19±0.025	4.20	33.92±1.29	1.65	0.284-2.272	0.9774

[a] Experiments were performed in a 10 mM Tris-HCl buffer at pH 7.4 containing 60 mM KCl; λ_{ex} = 434 nm.
[b] Relative fluorescence quantum yield of **BZT-Indolium** upon addition of c-MYC promoter G4-DNA at 9.0 μM. The standard of the relative fluorescence quantum yield is fluorescein (Φ_f = 0.95, methanol with 1% NaOH);
[c] Limit of detection for c-MYC promoter G4-DNA;
[d] Equilibrium binding constant between the compound and c-MYC promoter G4-DNA at 25 °C;
[e] Linear detection range of c-MYC promoter G4-DNA.

Table S4. Sequences of pu22 oligonucleotides used in the present study.

Abbreviation	Sequence (5′→3′)	Structure/origin
pu22	TGAGGGTGGGTAGGGTGGGTAA	G-quadruplex
pu22/A3T	TG**T**GGGTGGGTAGGGTGGGTAA	G-quadruplex
pu22/A3C	TG**C**GGGTGGGTAGGGTGGGTAA	G-quadruplex
pu22/A3G	TG**G**GGGTGGGTAGGGTGGGTAA	G-quadruplex
pu22/T7A	TGAGGG**A**GGGTAGGGTGGGTAA	G-quadruplex
pu22/ T7C	TGAGGG**C**GGGTAGGGTGGGTAA	G-quadruplex
pu22/ T7G	TGAGGG**G**GGGTAGGGTGGGTAA	G-quadruplex
pu22/ T11A	TGAGGGTGGG**A**AGGGTGGGTAA	G-quadruplex
pu22/ T11C	TGAGGGTGGG**C**AGGGTGGGTAA	G-quadruplex
pu22/ T11G	TGAGGGTGGG**G**AGGGTGGGTAA	G-quadruplex
pu22/ A12C	TGAGGGTGGGT**C**GGGTGGGTAA	G-quadruplex
pu22/ A12G	TGAGGGTGGGT**G**GGGTGGGTAA	G-quadruplex

pu22/ A12T	TGAGGGTGGGT**T**GGGTGGGTAA	G-quadruplex
pu22/ T16A	TGAGGGTGGGTAGGG**A**GGGTAA	G-quadruplex
pu22/ T16C	TGAGGGTGGGTAGGG**C**GGGTAA	G-quadruplex
pu22/ T16G	TGAGGGTGGGTAGGG**G**GGGTAA	G-quadruplex
An illustration model of pu22 G4-DNA	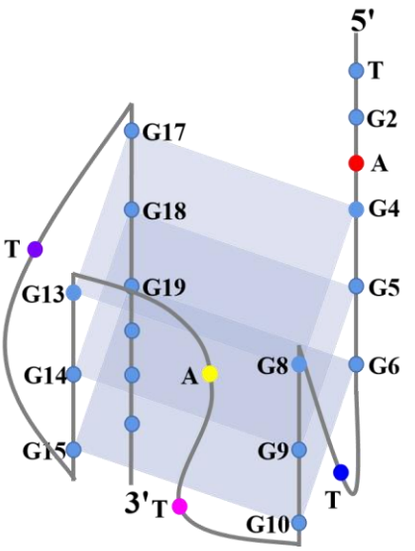	

Table S5. IC_{50} of **BZT-Indolium** against the cell lines.[a]

Cell lines	IC_{50} (μM)
U87	20.18±0.76
HeLa	8.68±1.15
MCF7	11.41±1.34
16HBE	25.15±0.68
HK2	33.68±0.97

[a] Data are presented in mean±SD of three independence experiments and each was performed in triplicate.

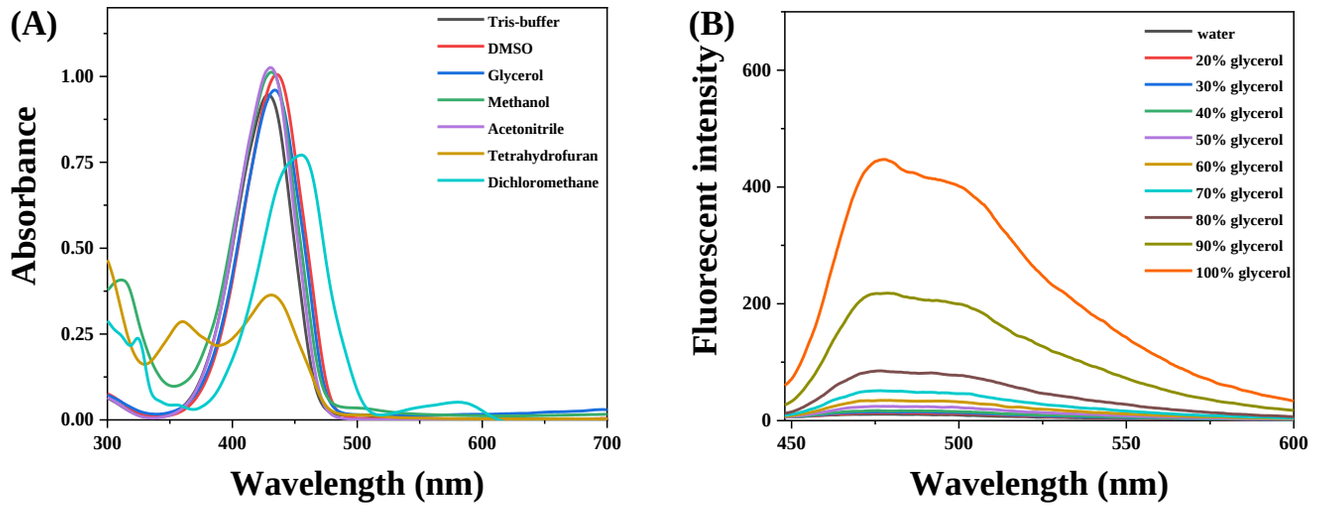

Figure S1. (A) Absorption spectra of 20 μM of **BZT-Indolium** in different solvents, including Tris-buffer, DMSO, glycerol, methanol, acetonitrile, tetrahydrofuran and dichloromethane; (B) Fluorescent intensity of **BZT-Indolium** in different glycerol ratios. The concentration of the compound was 0.5 μM.

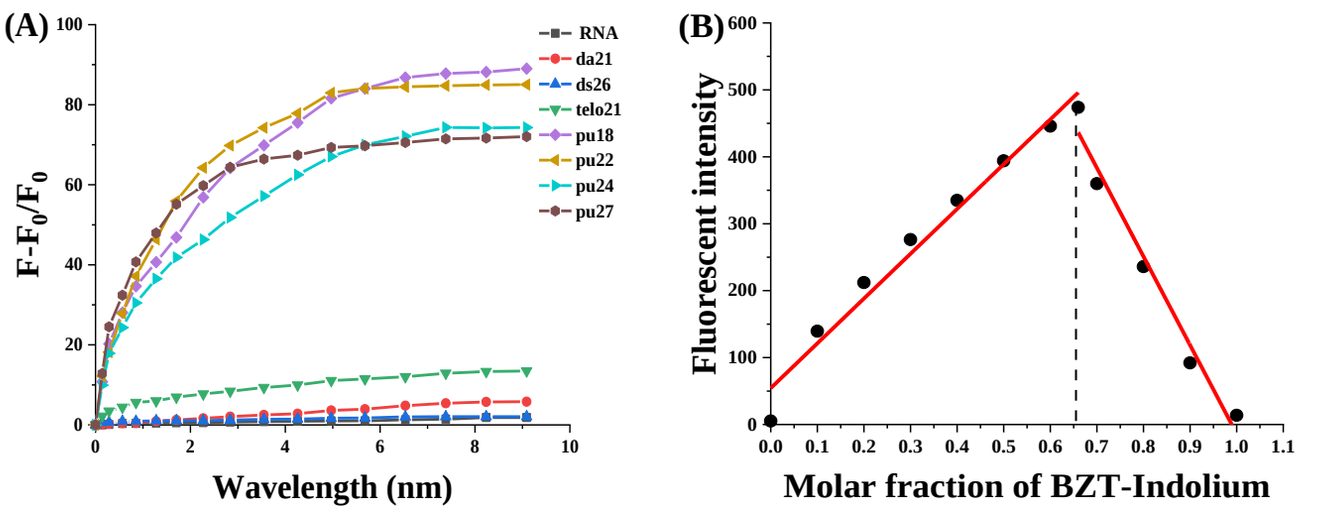

Figure S2. (A) Fluorescence titration of the probe **BZT-Indolium** with different concentrations of RNA, da21, ds26, telo21, pu18, pu22, pu24 and pu27. Fluorescence signal was measured at 25 °C, and the concentration of **BZT-Indolium** was 0.5 μM in Tris−HCl buffer (10 mM, pH 7.4) containing 60 mM KCl. F_0 represents the fluorescence intensity of **BZT-Indolium** itself, and F represents the maximum fluorescence intensity of **BZT-Indolium** after binding with nucleic acids. (B) Job plot analysis of binding stoichiometry of **BZT-Indolium** and pu27.

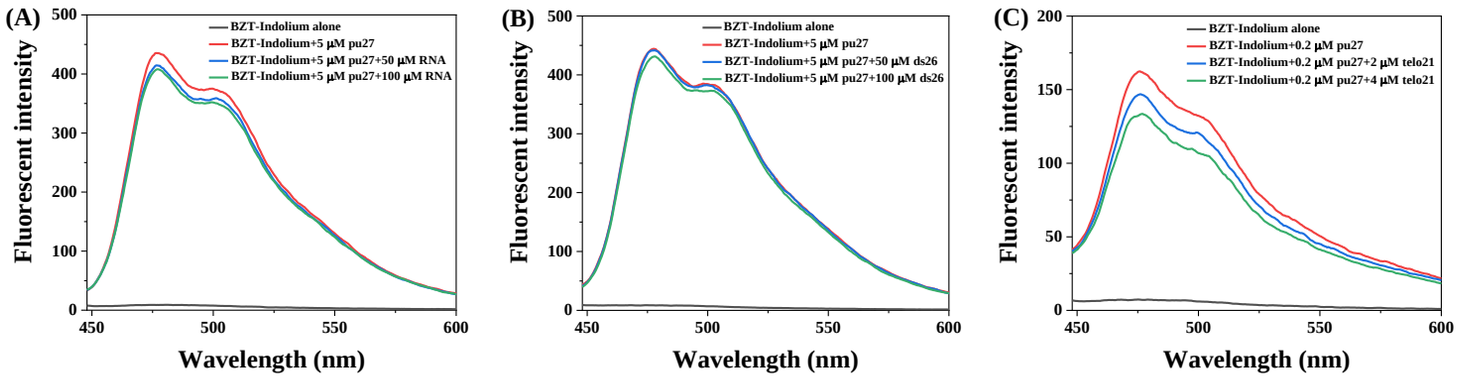

Figure S3. *In vitro* competition study of **BZT-Indolium** between pu27 G4-DNA and other nucleic acids: (A) pu27 at 5 μM and RNA was added at the concentrations 50 μM and 100 μM; (B) pu27 at 5 μM and double-stranded DNA (ds26) was added at the concentrations 50 μM and 100 μM; (C) pu27 at 0.2 μM and telo21 G4-DNA was added at the concentrations 2 μM and 4 μM. The concentration of **BZT-Indolium** was 0.5 μM in Tris−HCl buffer (10 mM, pH 7.4) containing 60 mM KCl.

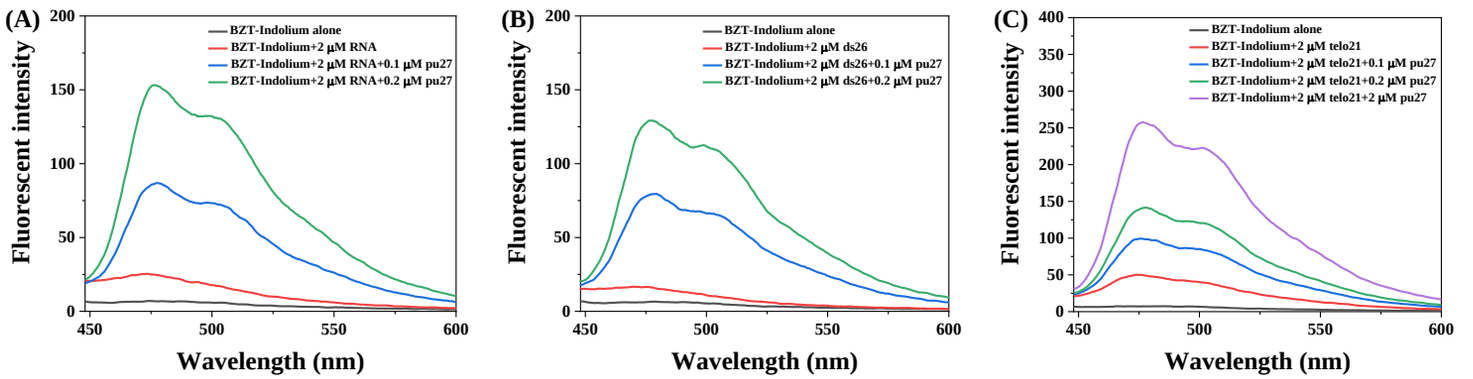

Figure S4. *In vitro* competition study of **BZT-Indolium** between pu27 G4-DNA and other nucleic acids: (A) 0.1 and 0.2 μM pu27 G4-DNA was added subsequently to compete with RNA at 2 μM; (B) 0.1 and 0.2 μM pu27 G4-DNA was added subsequently to compete with double-strand DNA (ds26) at 2 μM; (C) 0.1, 0.2 and 2 μM pu27 G4-DNA was added subsequently to compete with telo21 G4-DNA at 2 μM. The concentration of **BZT-Indolium** was 0.5 μM in Tris−HCl buffer (10 mM, pH 7.4) containing 60 mM KCl.

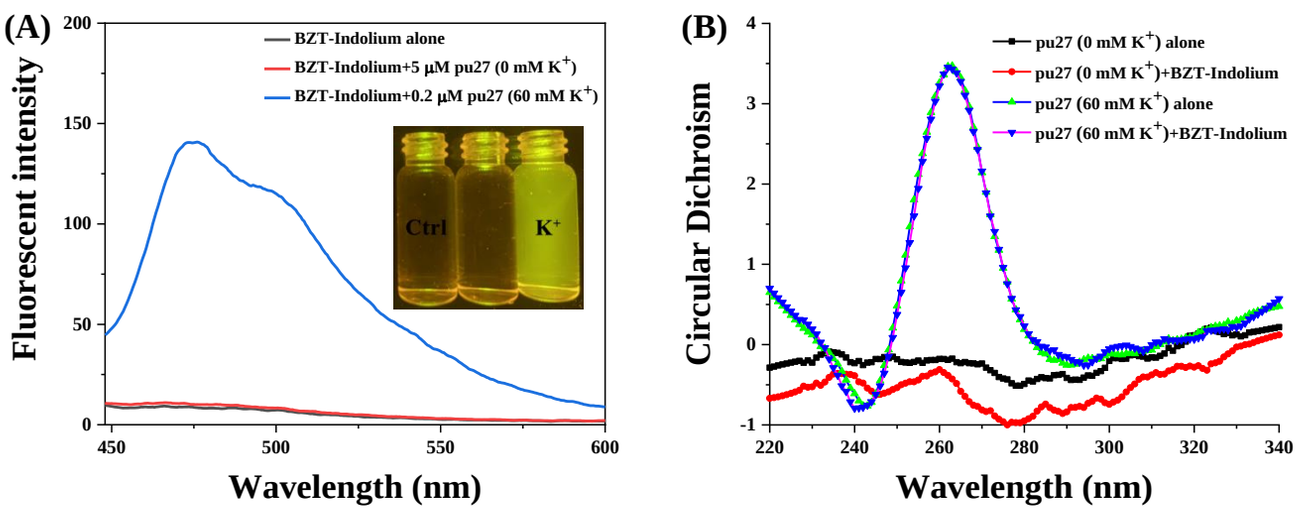

Figure S5. Study of conformational effects of **BZT-Indolium** on the G4-structure: (A) Fluorescence response of **BZT-Indolium** to K^+ free pu27 G4-DNA and pu27 G4-DNA which contains 60 mM K^+ was added subsequently, the concentration ratio is 10/1. (B) CD spectra of pu27 (5 μM) interacted with the probe without K^+ ion and with 60 mM KCl in 10 mM Tris-HCl buffer at pH 7.4.

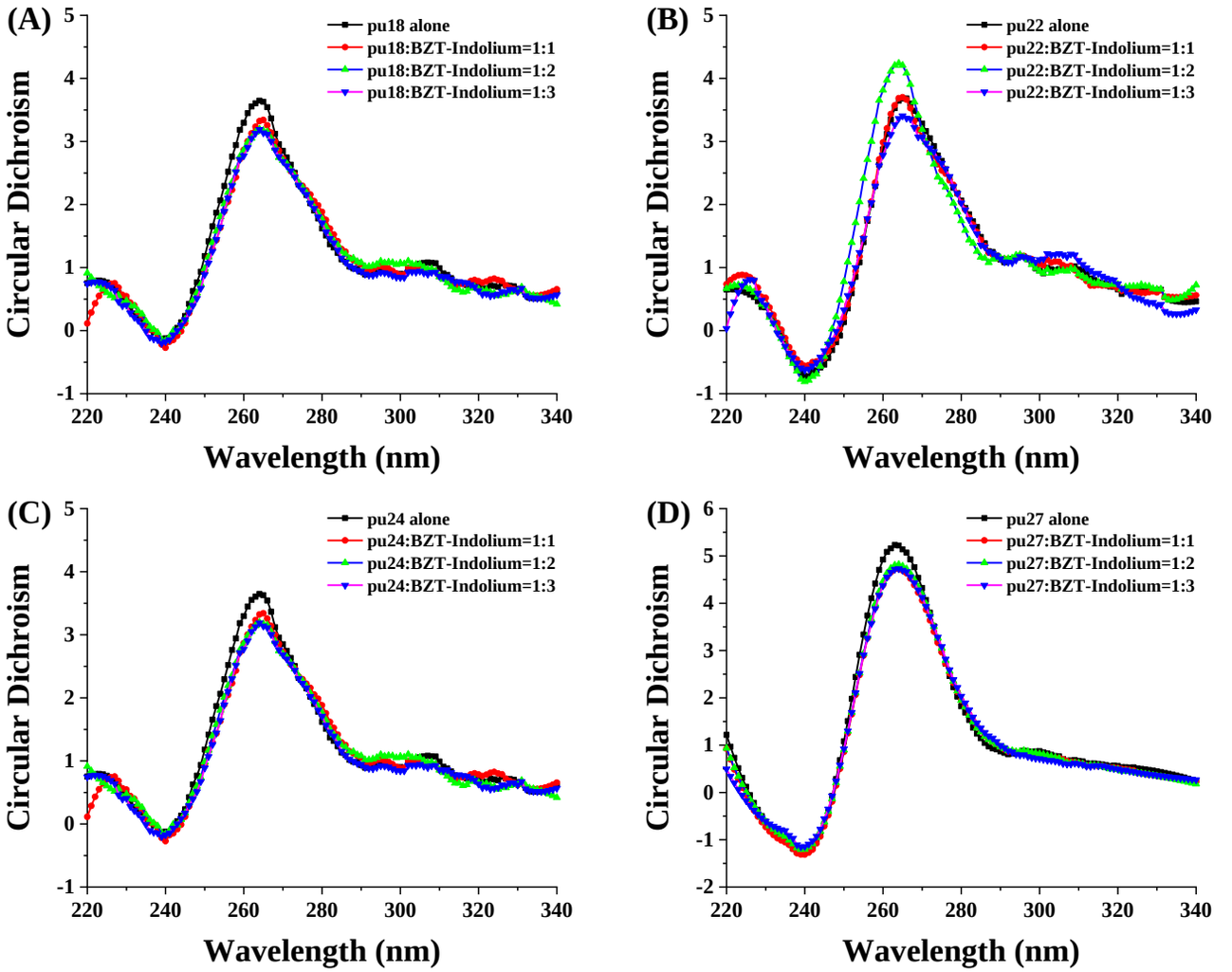

Figure S6. CD spectra of c-MYC G4-DNA (5 μM) interacted with different concentration of **BZT-Indolium** (1 to 3 equivalents) in 10 mM Tris-HCl buffer with 60 mM KCl at pH 7.4: (A) pu18; (B) pu22; (C) pu24; and (D) pu27.

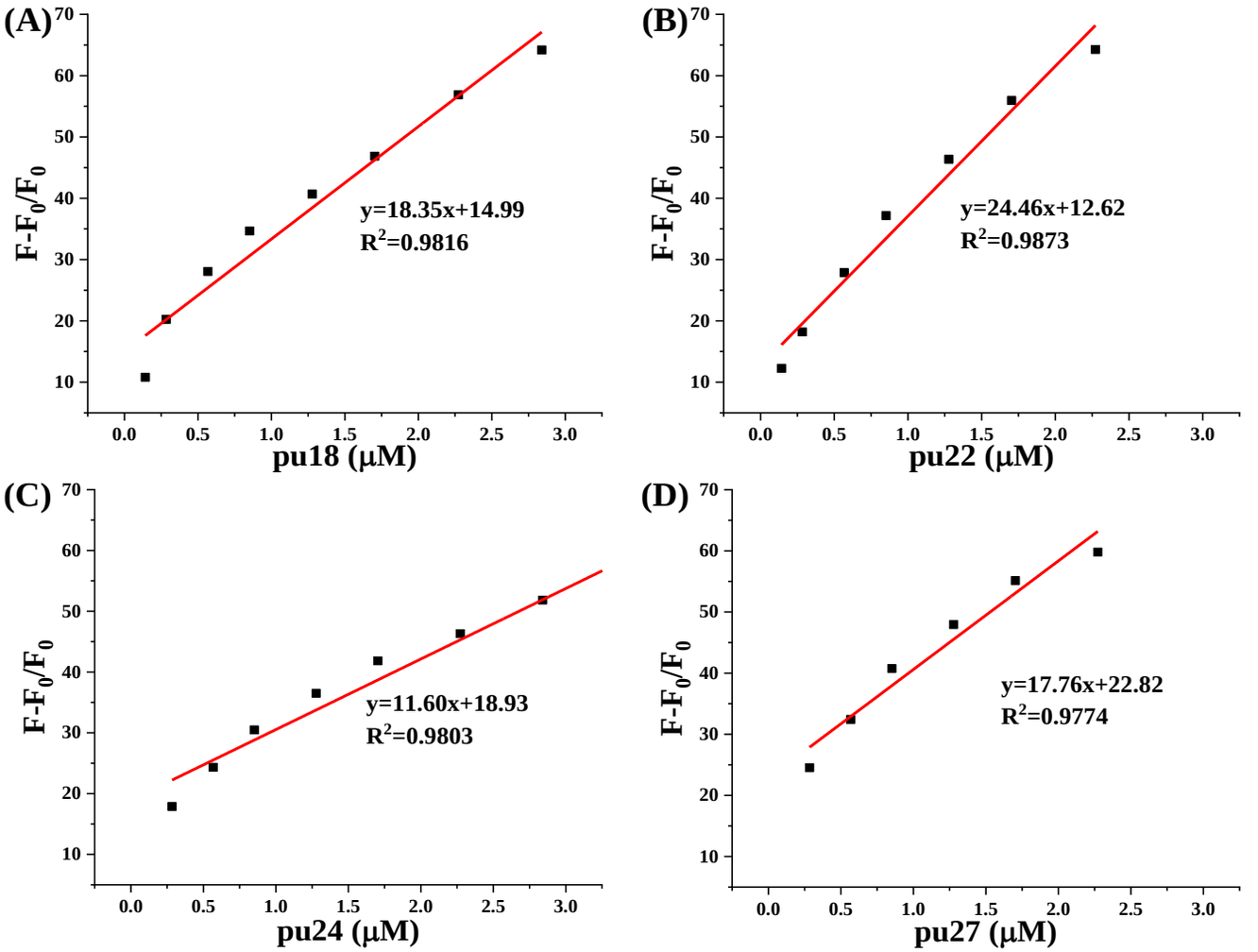

Figure S7. (A) Linear relationship of probe **BZT-Indolium** in the detection of pu18; (B) Linear relationship of probe **BZT-Indolium** in the detection of pu22; (C) Linear relationship of probe **BZT-Indolium** in the detection of pu24; (D) Linear relationship of probe **BZT-Indolium** in the detection of pu27. The concentration of **BZT-Indolium** was 0.5 μM in Tris−HCl buffer (10 mM, pH 7.4) containing 60 mM KCl.

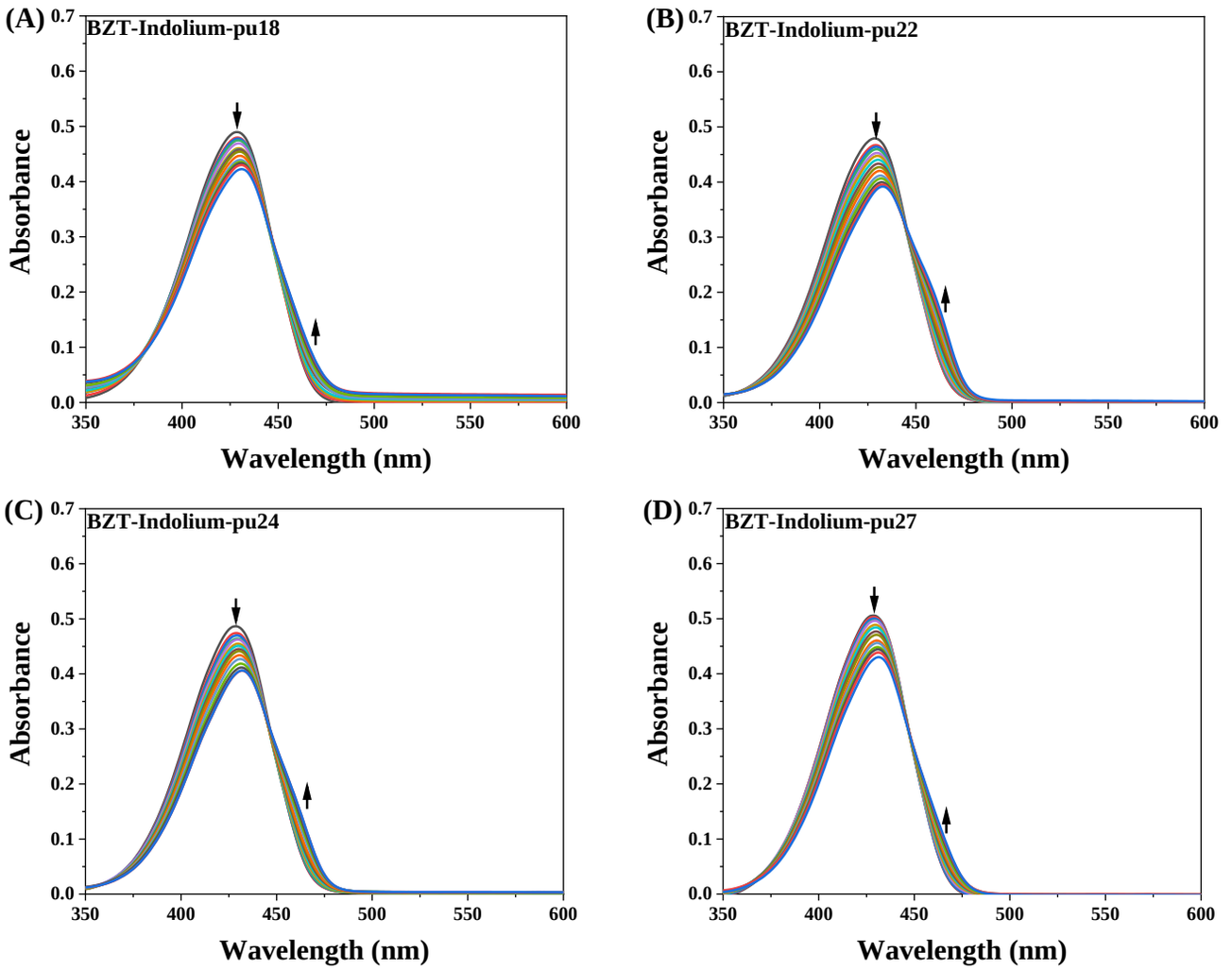

Figure S8. UV-vis titration spectra of **BZT-Indolium** (10 μM) with different concentration of c-MYC G4-DNA in a Tris-HCl buffer (10 mM, pH = 7.4) with 60 mM KCl: (A) pu18; (B) pu22; (C) pu24; and (D) pu27.

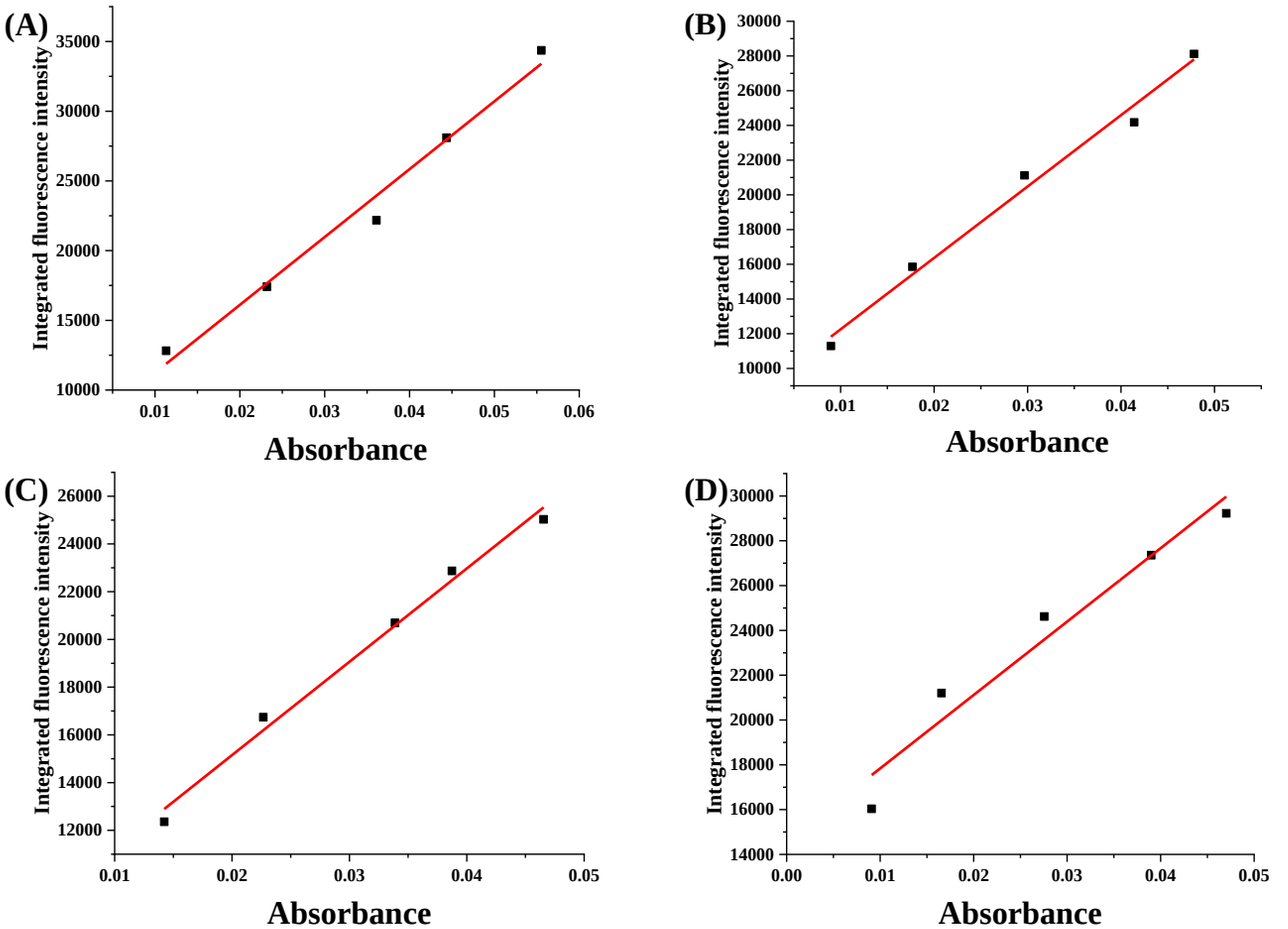

Figure S9. (A) The linear fitting of the absorption intensity by the fluorescence emission spectral integral area of **BZT-Indolium** in pu18; (B) The linear fitting of the absorption intensity by the fluorescence emission spectral integral area of **BZT-Indolium** in pu22; (C) The linear fitting of the absorption intensity by the fluorescence emission spectral integral area of **BZT-Indolium** in pu24; (D) The linear fitting of the absorption intensity by the fluorescence emission spectral integral area of **BZT-Indolium** in pu27. The concentration of **BZT-Indolium** was 0.5 μM in Tris−HCl buffer (10 mM, pH 7.4) containing 60 mM KCl.

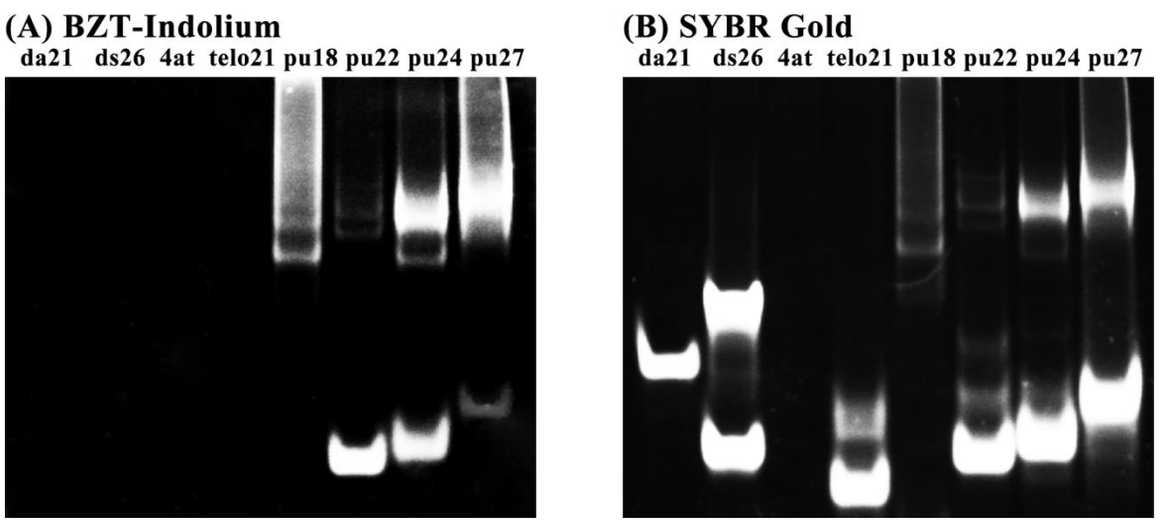

Figure S10. (A) Gel electrophoresis (20 % acrylamide in 1 × TBE) of da21, ds26, 4at, telo21, pu18, pu22, pu24, pu27 at a concentration of 5.0 μM and was stained with **BZT-Indolium** (5.0 μM) for 15 min; (B) Gel electrophoresis (20 % acrylamide in 1 × TBE) of da21, ds26, 4at, telo21, pu18, pu22, pu24, pu27 at a concentration of 5.0 μM and was stained with **SYBR Gold** (5.0 μM) for 15 min.

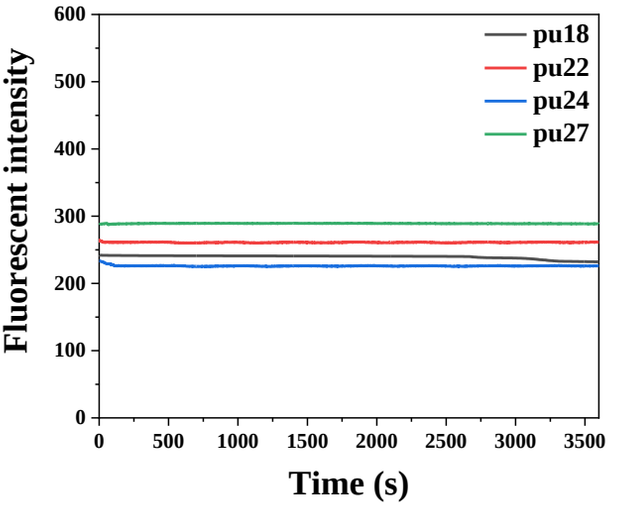

Figure S11. The curve of fluorescence intensity with time (1 h) after the combination of probe **BZT-Indolium** (0.5 μM) with c-MYC promoter G4-DNA (pu18, pu22, pu24, pu27) (1.0 μM). The excitation wavelength λ_{ex} = 434 nm, the emission wavelength λ_{em} = 477 nm.

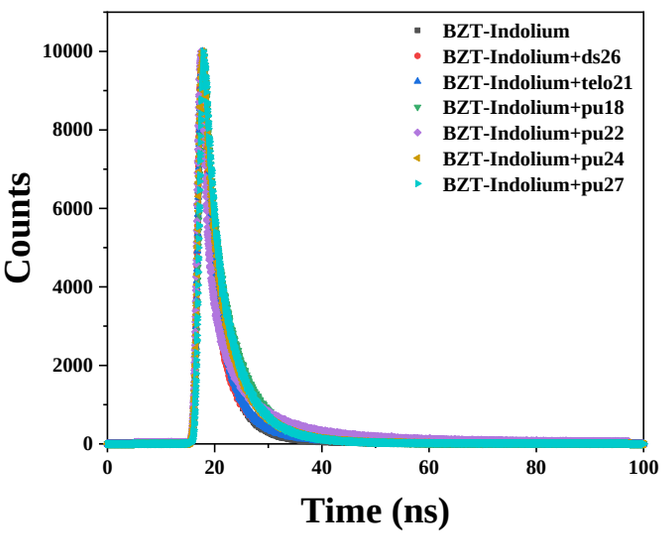

DNA-Probe complex	τ1 (ns)	τ2 (ns)	lifetime (ns)
BZT-Indolium (control)	2.06	5.08	**3.05**
Duplex DNA (ds26)	2.28	9.32	3.28
Telomere G4-DNA (telo21)	2.51	7.26	3.42
c-MYC G4-DNA (pu18)	2.12	6.18	**4.49**
c-MYC G4-DNA (pu22)	2.08	6.32	**4.07**
c-MYC G4-DNA (pu24)	2.39	6.20	**4.12**
c-MYC G4-DNA (pu27)	2.13	5.72	**4.20**

Figure S12. Fluorescence decay traces of **BZT-Indolium** (0.5 μM, λ_{ex} = 320 nm, λ_{em} = 477 nm) in the absence and in the presence of different DNA substrates including ds26, telo21, pu18, pu22, pu24 and pu27 in 10 mM Tris-HCl buffer at pH 7.4 containing 60 mM KCl.

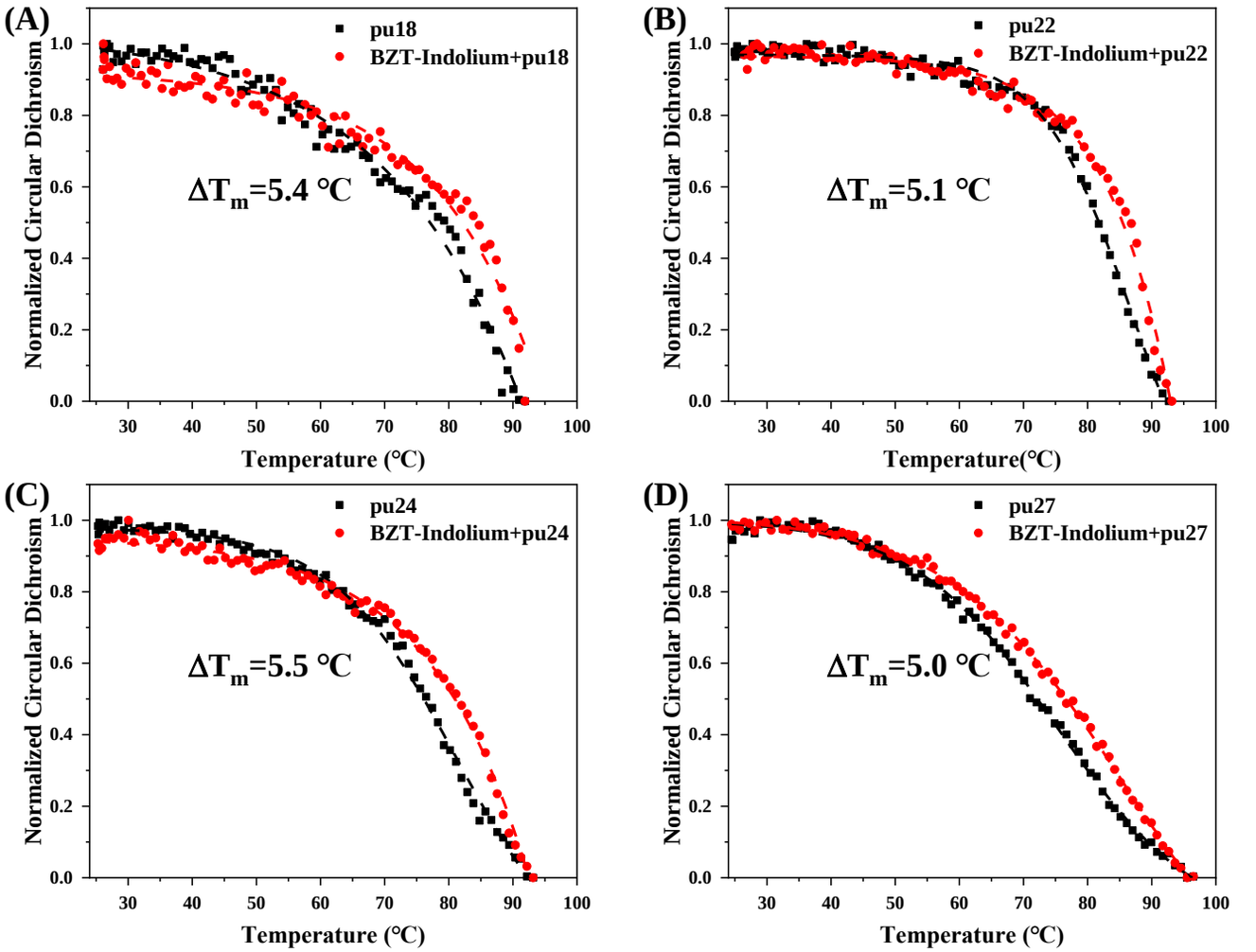

Figure S13. The evaluation the G4-structure stabilization ability of **BZT-Indolium** in 10 mM Tris-HCl buffer at pH 7.4 containing 60 mM KCl: (A) Normalized CD signal of pu18 during melting process; (B) Normalized CD signal of pu22 during melting process; (C) Normalized CD signal of pu24 during melting process; (D) Normalized CD signal of pu27 during melting process. The G-quadruplex was characterized by the positive peak at 262 nm.

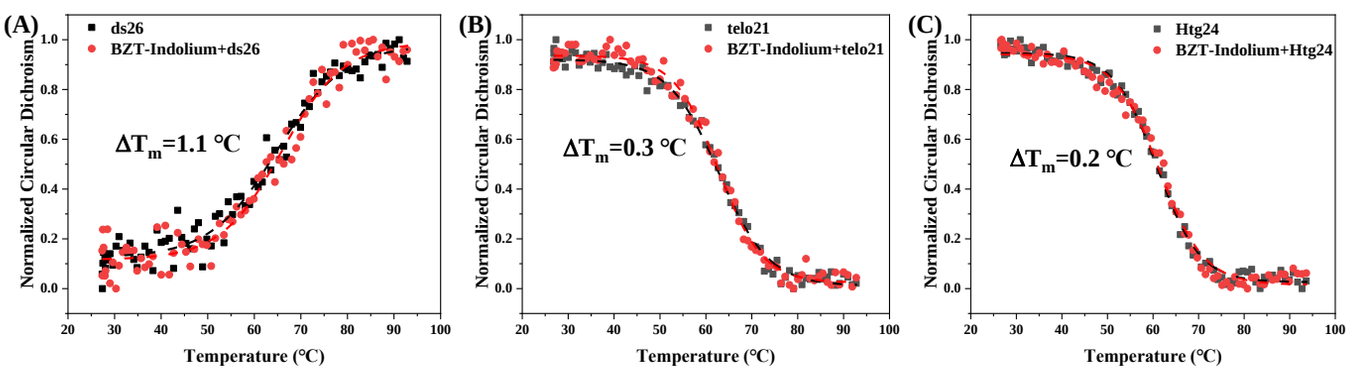

Figure S14. The evaluation the stabilization ability of **BZT-Indolium** in 10 mM Tris-HCl buffer at pH 7.4 containing 60 mM KCl: (A) Normalized CD signal of double stranded DNA (ds26) during melting process, the double stranded DNA was characterized by the negative peak at 242 nm; (B) Normalized CD signal of Telomere G4-DNA (telo21) during melting process, the G-quadruplex was characterized by the positive peak at 290 nm; (C) Normalized CD signal of Telomere G4-DNA (Htg24) during melting process, the G-quadruplex was characterized by the positive peak at 290 nm.

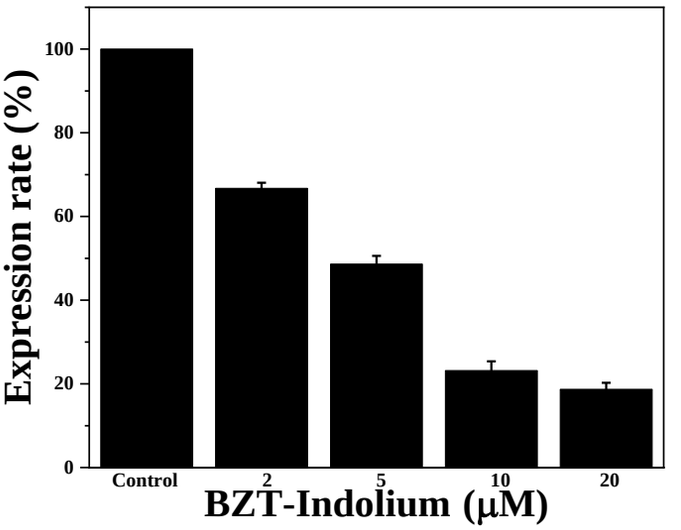

Figure S15. Expression rate of c-MYC mRNA at different concentrations of **BZT-Indolium**.

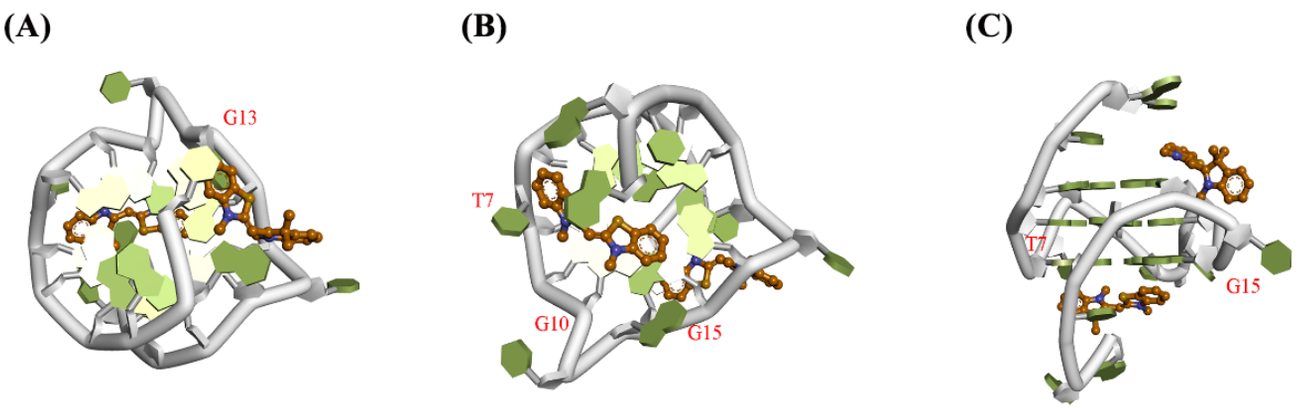

Figure S16. The molecular docking study of **BZT-Indolium** in complex with pu22 G-quadruplex. Top view (A), bottom view (B) and side view (C) of **BZT-Indolium** in complex with pu22 G-quadruplex in a 2:1 binding mode. Residues involved in the ligand-G4 interactions were highlighted.

The molecular docking results of **BZT-Indolium** in complex with pu22 G-quadruplex in 2:1 binding mode were shown in **Figure S16**. At the 5' end planar, the benzothiazole scaffold of **BZT-Indolium** is able to stack on the pu22 G4 mainly by pi-pi stacking with G13 and T1 residues, while the methylquinolinium with two methyl group is pointing out of the G4 structure. At the 3' end planar, the benzothiazole group is pi-pi stacking with G10 and G15 residues, while the methylquinolinium structure is pi-pi stacking with T7 loop. The result of molecular docking is consistent with the NMR titration and fluorescence binding assays.

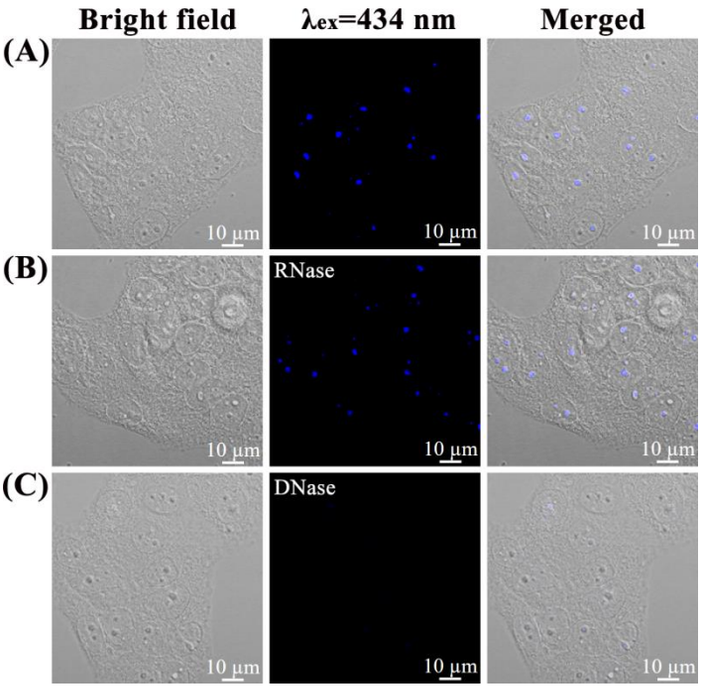

Figure S17. (A) Fluorescence images of live MCF-7 cells stained with 5.0 μM **BZT-Indolium** for 15 min; (B) Fluorescence images of live MCF-7 cells stained with 5.0 μM **BZT-Indolium** for 15 min and RNase treated for 2 h; (C) Fluorescence images of live MCF-7 cells stained with 5 μM **BZT-Indolium** for 15 min and DNase treated for 2 h.

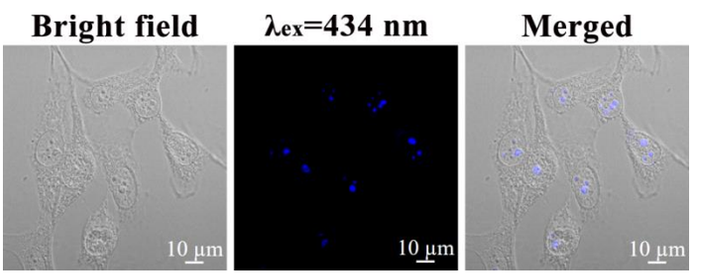

Figure S18. Fluorescence images of live normal cells 16HBE stained with 5.0 μM **BZT-Indolium** for 15 min.

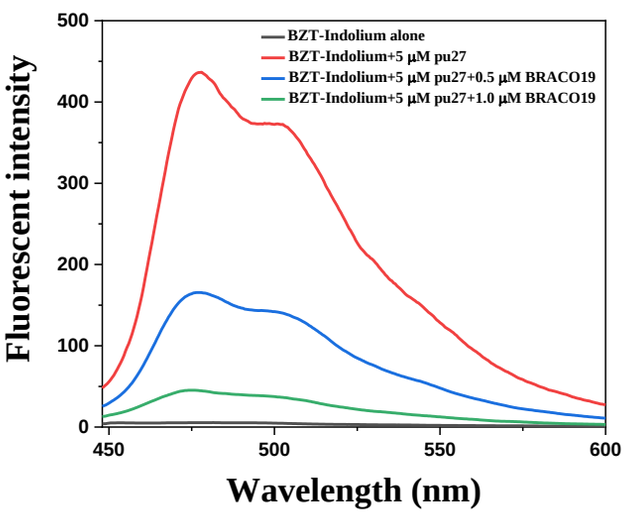

Figure S19. Fluorescence response of **BZT-Indolium** (0.5 μM) added to pu27 G4-DNA and BRACO19 was added subsequently. The concentration ratio between **BZT-Indolium** and BRACO19 is 1: 1 and 1: 2.

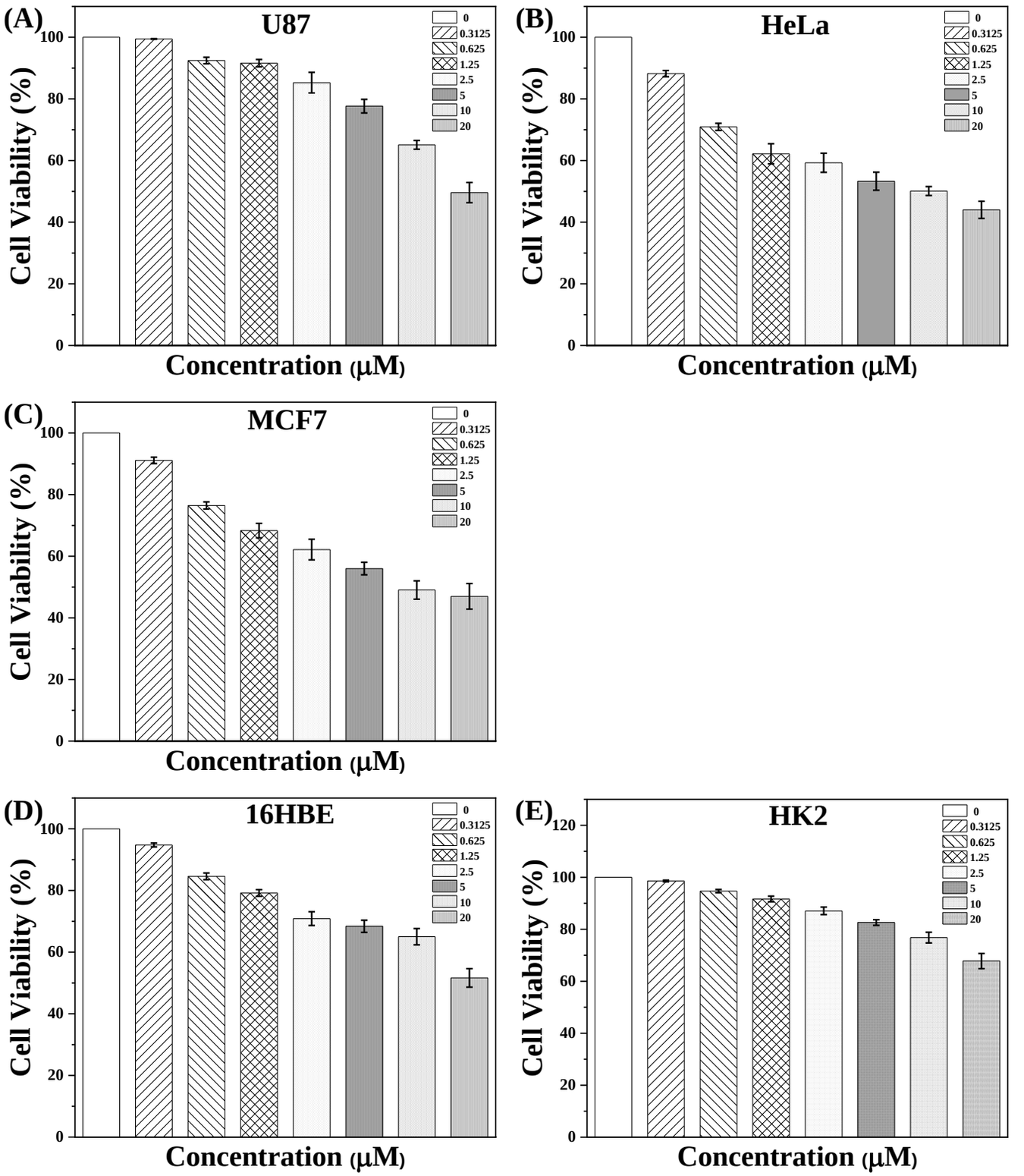

Figure S20. (A) Cells survival viability of U87 cells; (B) Cells survival viability of HeLa cells; (C) Cells survival viability of MCF7 cells; (D) Cells survival viability of 16HBE cells; (E) Cells survival viability of HK2 cells. The concentration gradients of **BZT-Indolium** were 0, 0.3125, 0.625, 1.25, 5, 10 and 20 μM.

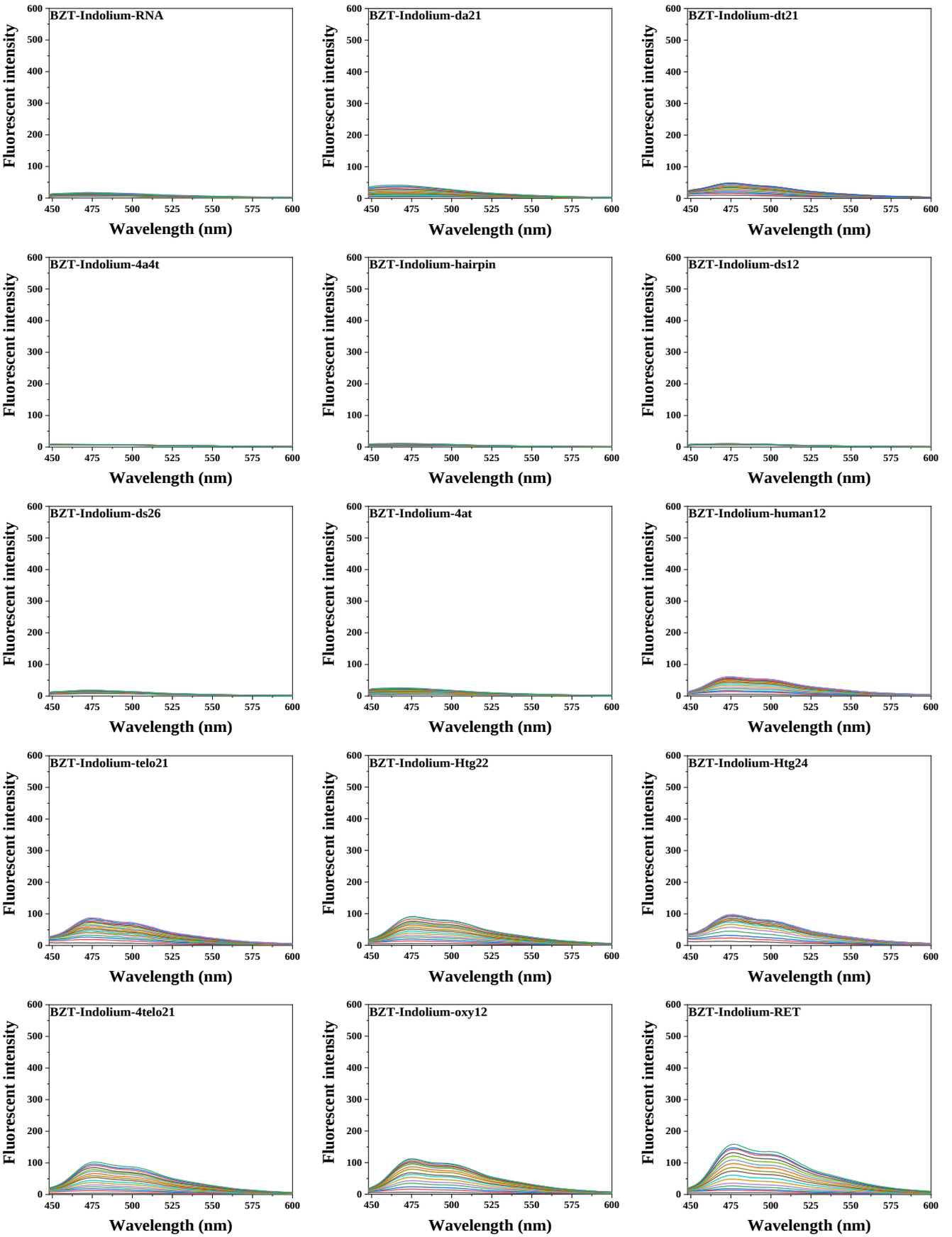
BZT-Indolium-RNA
BZT-Indolium-da21
BZT-Indolium-dt21
BZT-Indolium-4a4t
BZT-Indolium-hairpin
BZT-Indolium-ds12
BZT-Indolium-ds26
BZT-Indolium-4at
BZT-Indolium-human12
BZT-Indolium-telo21
BZT-Indolium-Htg22
BZT-Indolium-Htg24
BZT-Indolium-4telo21
BZT-Indolium-oxy12
BZT-Indolium-RET
Fluorescent intensity
Wavelength (nm)
0
100
200
300
400
500
600
450
475
500
525
550
575
600

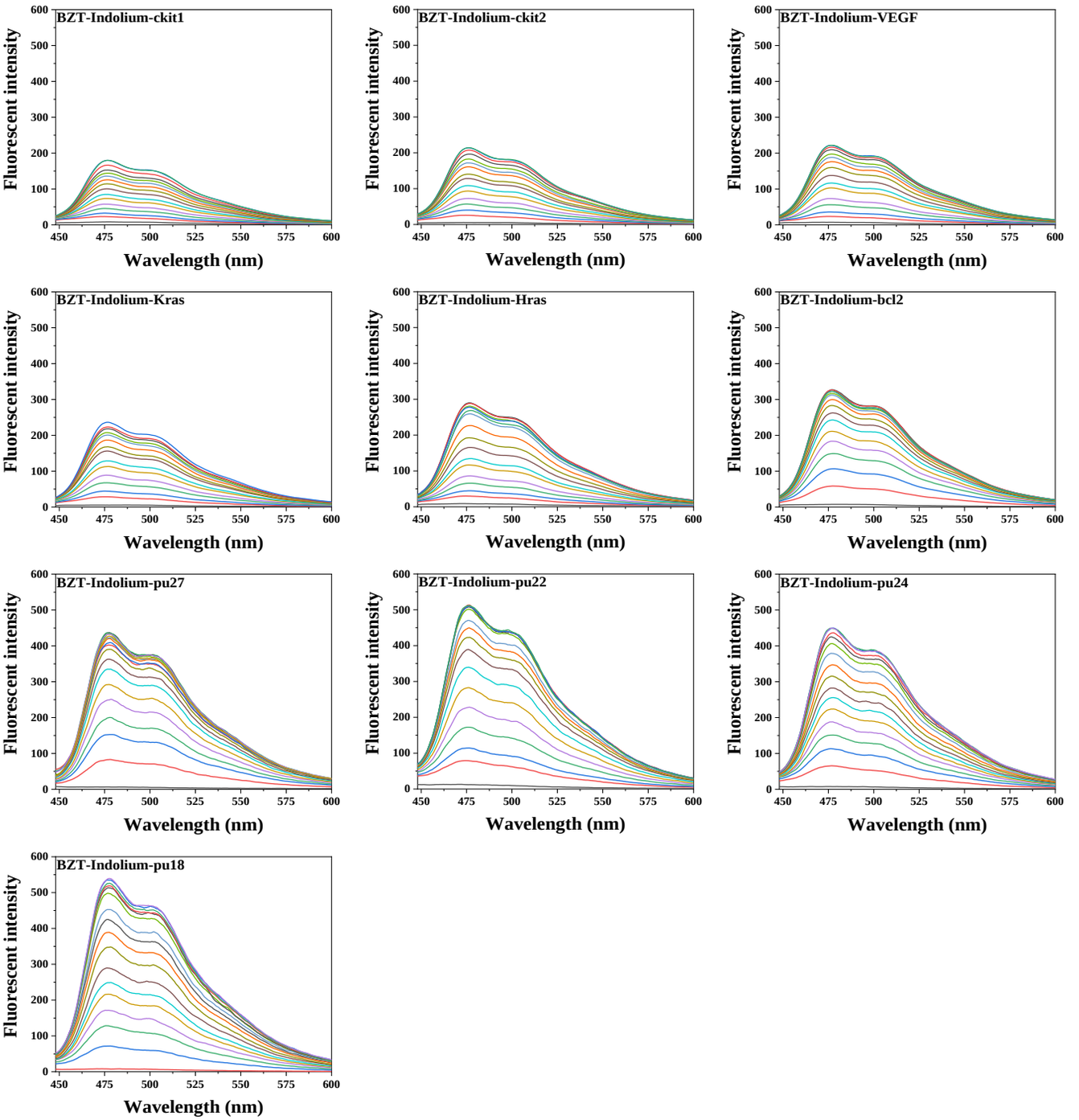

Figure S21. Fluorescence titration spectra of **BZT-Indolium** with different nucleic acids: RNA; single-stranded DNA: da21, dt21; duplex DNA: 4a4t, hairpin, ds12, ds26, 4at; Telomere G4-DNA: human12, telo21, Htg22, Htg24, 4telo21, oxy12; Promoter G4-DNA: RET, ckit1, ckit2, VEGF, Kras, Hras, bcl2, pu18, pu22, pu24 and pu27 in a Tris-HCl buffer (10 mM, pH 7.4) containing 60 mM KCl. Fluorescence signal was measured at 25 °C.

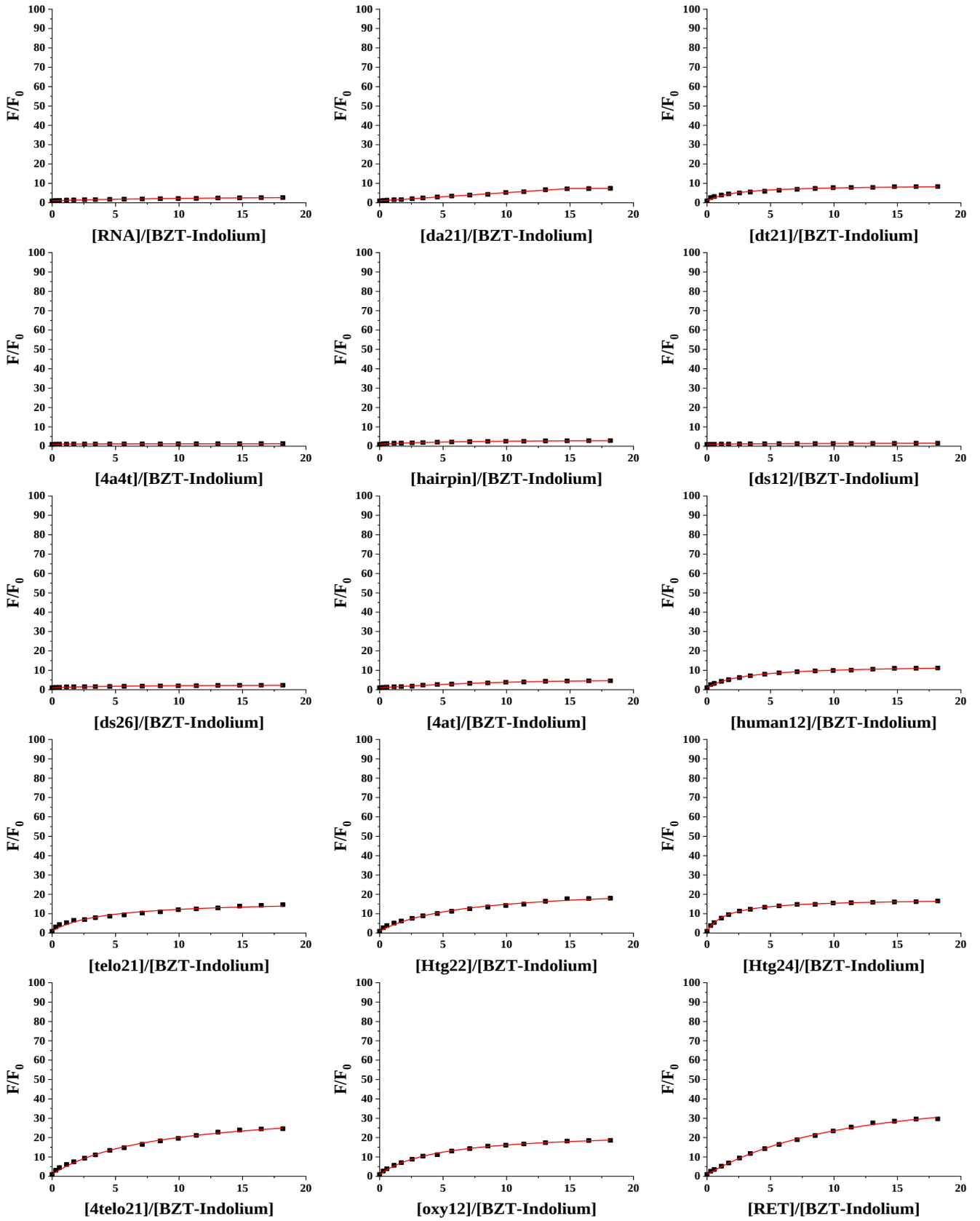
F/F0
[RNA]/[BZT-Indolium]
[da21]/[BZT-Indolium]
[dt21]/[BZT-Indolium]
[4a4t]/[BZT-Indolium]
[hairpin]/[BZT-Indolium]
[ds12]/[BZT-Indolium]
[ds26]/[BZT-Indolium]
[4at]/[BZT-Indolium]
[human12]/[BZT-Indolium]
[telo21]/[BZT-Indolium]
[Htg22]/[BZT-Indolium]
[Htg24]/[BZT-Indolium]
[4telo21]/[BZT-Indolium]
[oxy12]/[BZT-Indolium]
[RET]/[BZT-Indolium]

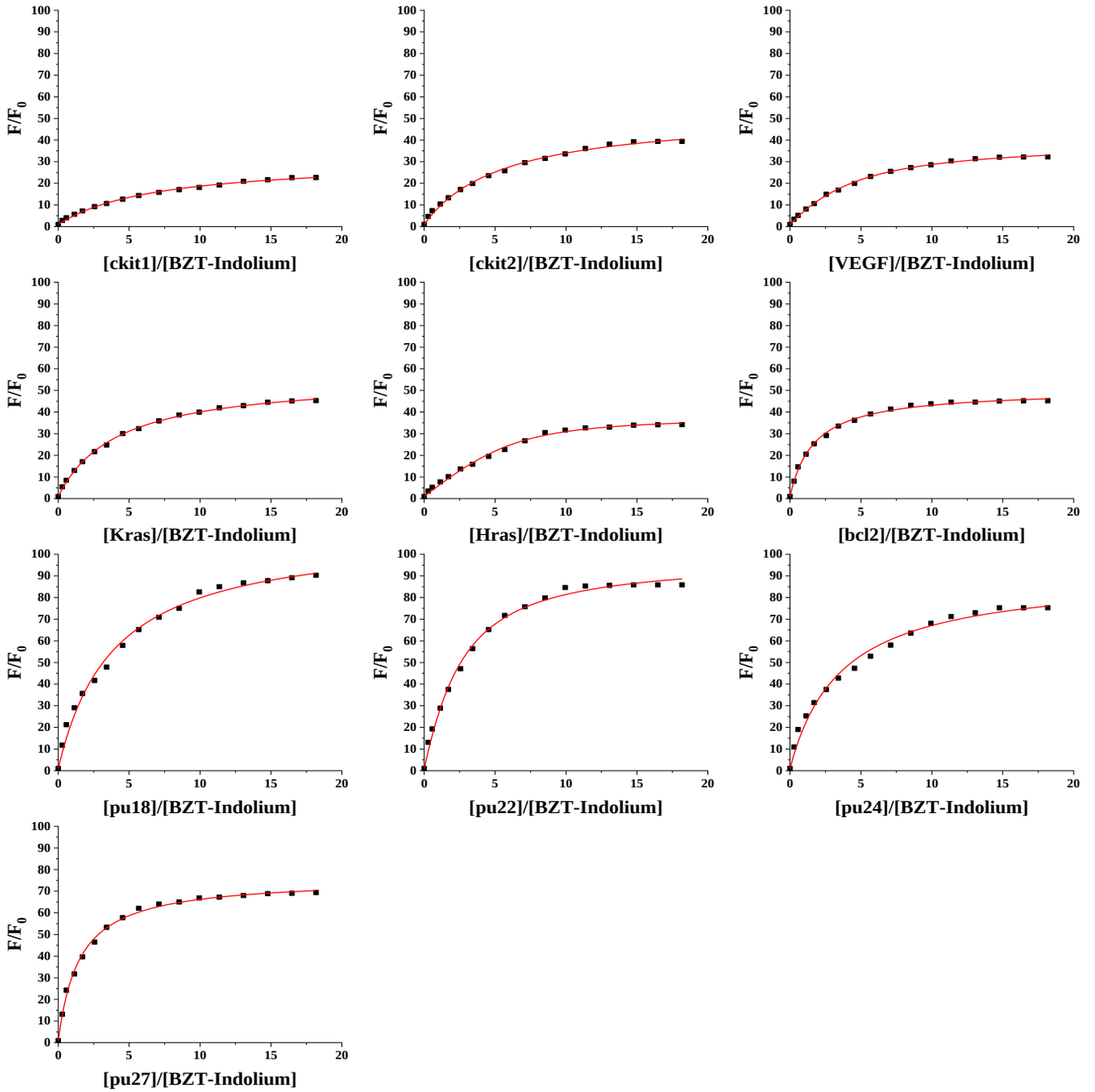

Figure S22. Fluorescence titrations, presented as a relative increase of the integral fluorescence (F/F_0) of different nucleic acids: RNA; single-stranded DNA: da21, dt21; duplex DNA: 4a4t, hairpin, ds12, ds26, 4at; Telomere G4-DNA: human12, telo21, Htg22, Htg24, 4telo21, oxy12; Promoter G4-DNA: RET, ckit1, ckit2, VEGF, Kras, Hras, bcl2, pu18, pu22, pu24 and pu27 with **BZT-Indolium** (0.5 μM) in 10 mM Tris-HCl buffer (pH 7.4, containing 60 mM KCl).

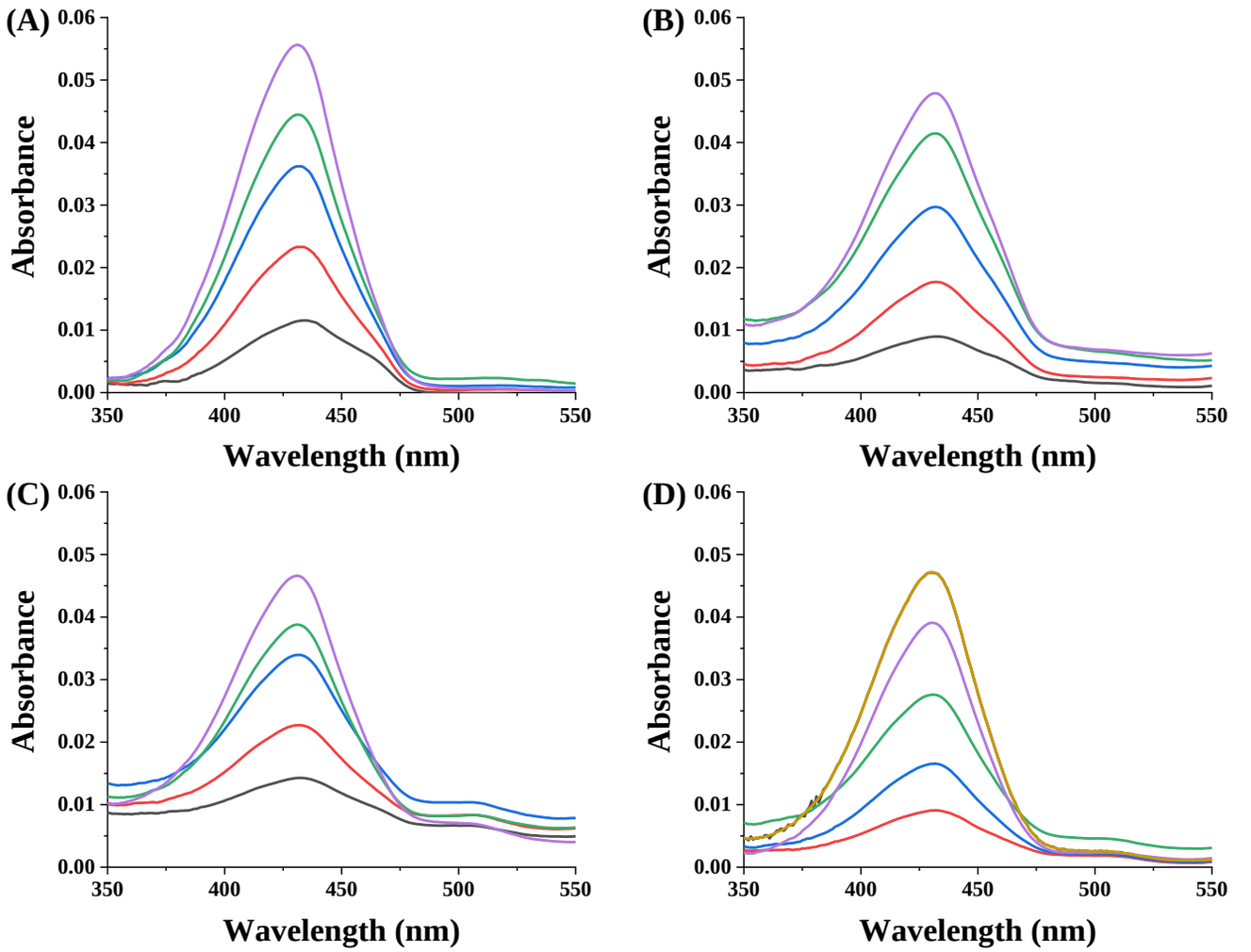

Figure S23. (A) The UV absorption spectrum obtained by adding five continuous concentrations (0.4 μM, 0.8 μM, 1.2 μM, 1.6 μM ,2.0 μM) of **BZT-Indolium** to a fixed concentration of 1 μM pu18; (B) The UV absorption spectrum obtained by adding five continuous concentrations (0.4 μM, 0.8 μM, 1.2 μM, 1.6 μM ,2.0 μM) of **BZT-Indolium** to a fixed concentration of 1 μM pu22; (C) The UV absorption spectrum obtained by adding five continuous concentrations (0.4 μM, 0.8 μM, 1.2 μM, 1.6 μM ,2.0 μM) of **BZT-Indolium** to a fixed concentration of 1 μM pu24; (D) The UV absorption spectrum obtained by adding five continuous concentrations (0.4 μM, 0.8 μM, 1.2 μM, 1.6 μM ,2.0 μM) of **BZT-Indolium** to a fixed concentration of 1 μM pu27.

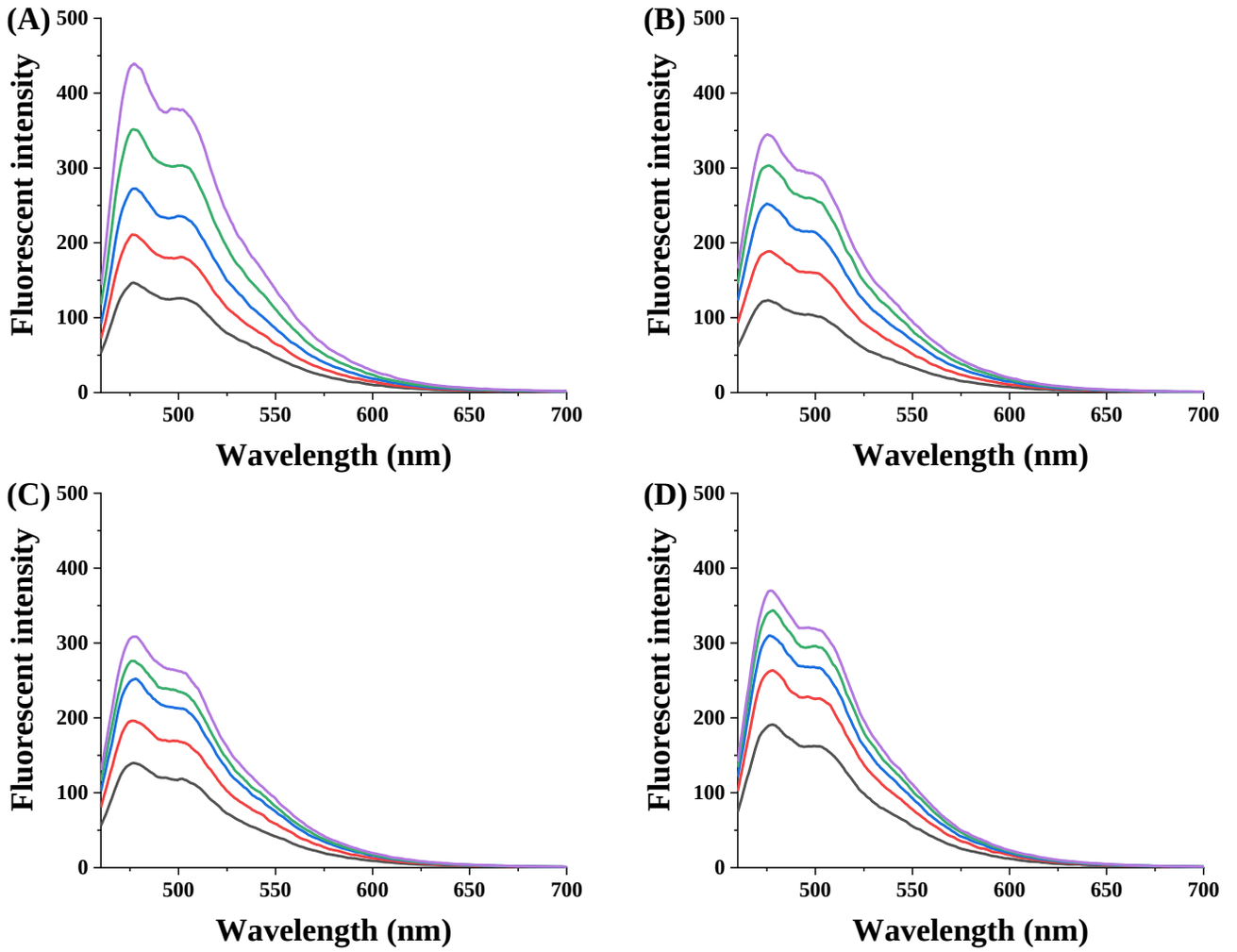

Figure S24. (A) Fluorescence spectrum obtained by adding five continuous concentrations of **BZT-Indolium** (0.4 μM, 0.8 μM, 1.2 μM, 1.6 μM ,2.0 μM) to a fixed concentration of 1 μM pu18; (B) Fluorescence spectrum obtained by adding five continuous concentrations of **BZT-Indolium** (0.4 μM, 0.8 μM, 1.2 μM, 1.6 μM ,2.0 μM) to a fixed concentration of 1 μM pu22; (C) Fluorescence spectrum obtained by adding five continuous concentrations of **BZT-Indolium** (0.4 μM, 0.8 μM, 1.2 μM, 1.6 μM ,2.0 μM) to a fixed concentration of 1 μM pu24; (D) Fluorescence spectrum obtained by adding five continuous concentrations (0.4 μM, 0.8 μM, 1.2 μM, 1.6 μM ,2.0 μM) of **BZT-Indolium** to a fixed concentration of 1 μM pu27.

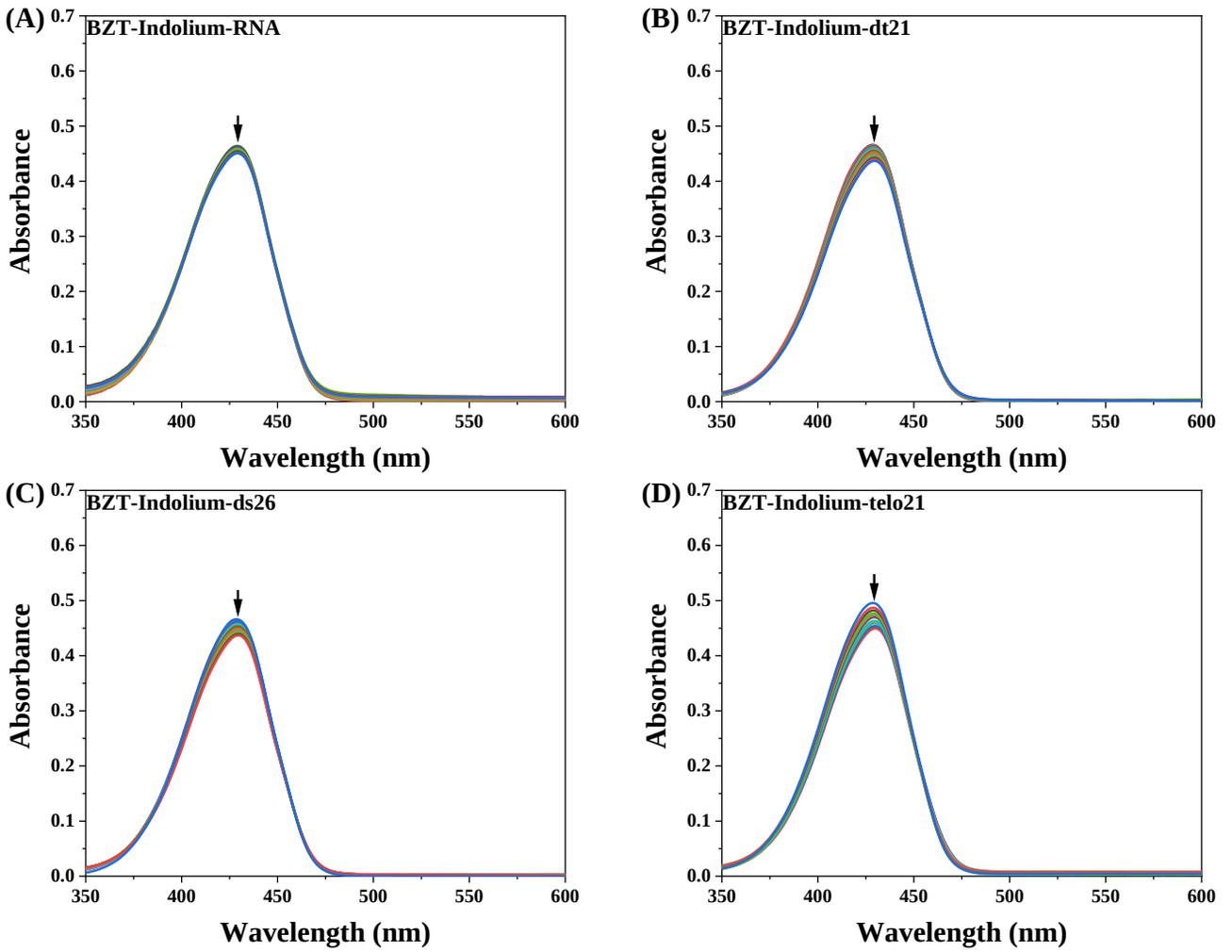

Figure S25. UV-vis titration spectra of **BZT-Indolium** (10 μM) with selected nucleic acids in a Tris-HCl buffer (10 mM, pH = 7.4) with 60 mM KCl at 25 °C: (A) RNA. (B) dt21. (C) ds26. (D) telo21 G4-DNA.

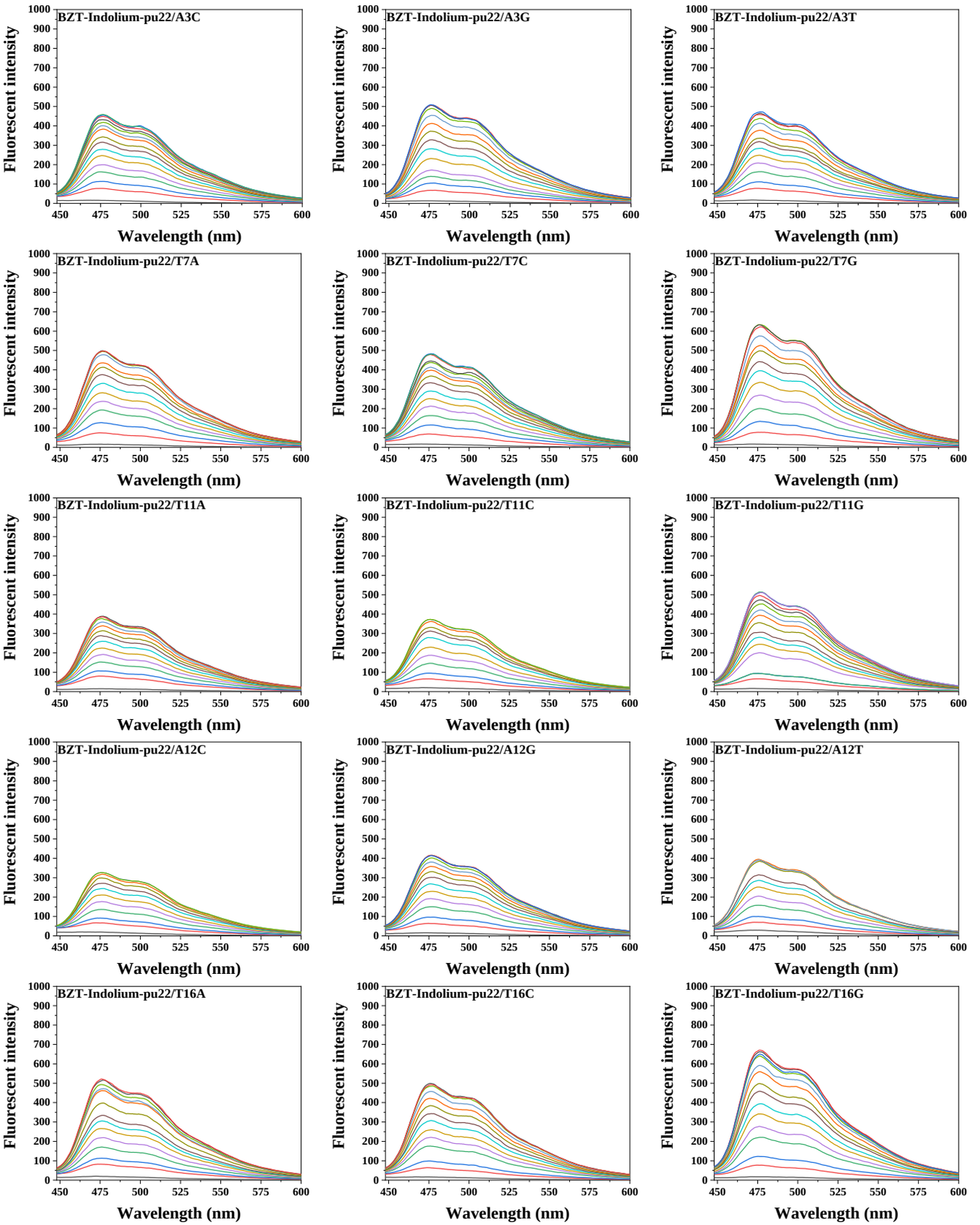

Figure S26. Fluorescence titration spectra of **BZT-Indolium** with different concentrations of pu22 mutants. The concentration of **BZT-Indolium** was 0.5 μM in Tris−HCl buffer (10 mM, pH 7.4) containing 60 mM KCl.

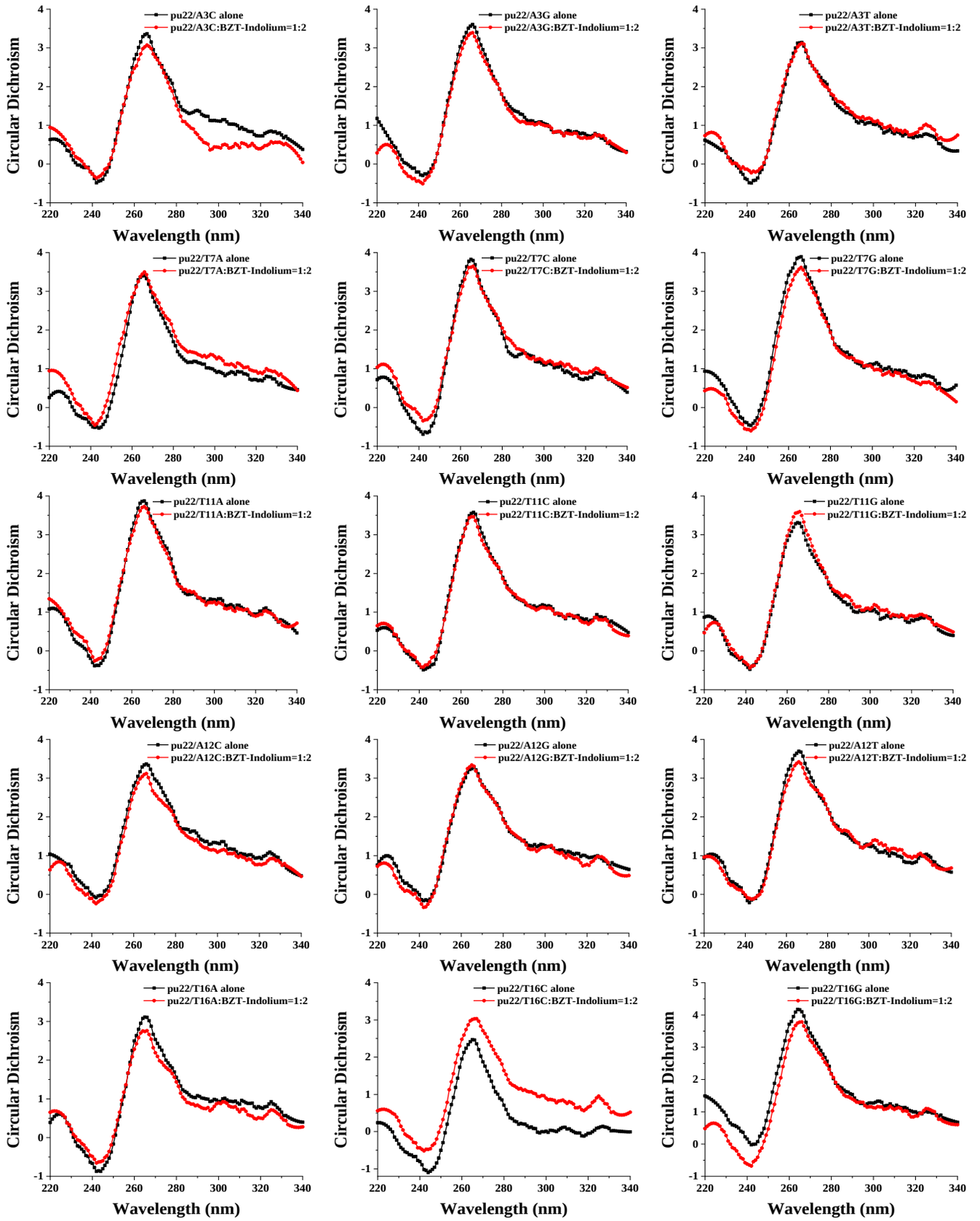

Figure S27. CD spectra of 5 μM pu22/A3C, pu18/A3G, pu22/A3T, pu22/T7A, pu22/T7C, pu22/T7G, pu22/T11A, pu22/T11C, pu22/T11G, pu22/A12C, pu22/A12G, pu22/A12T, pu22/T16A, pu22/T16C, pu22/T16G binding to **BZT-Indolium** in 10 mM Tris-HCl buffer at pH 7.4 with 60 mM KCl.

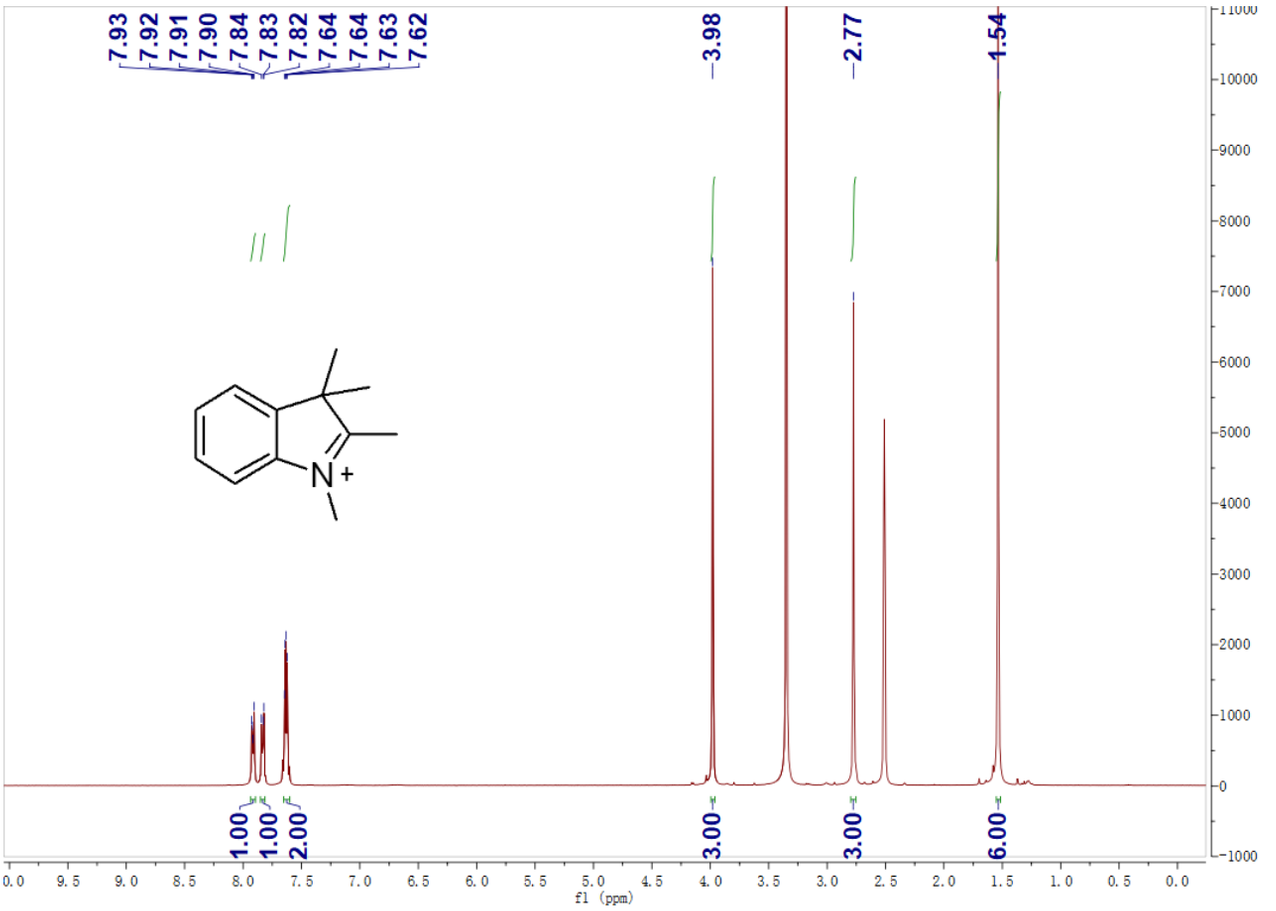

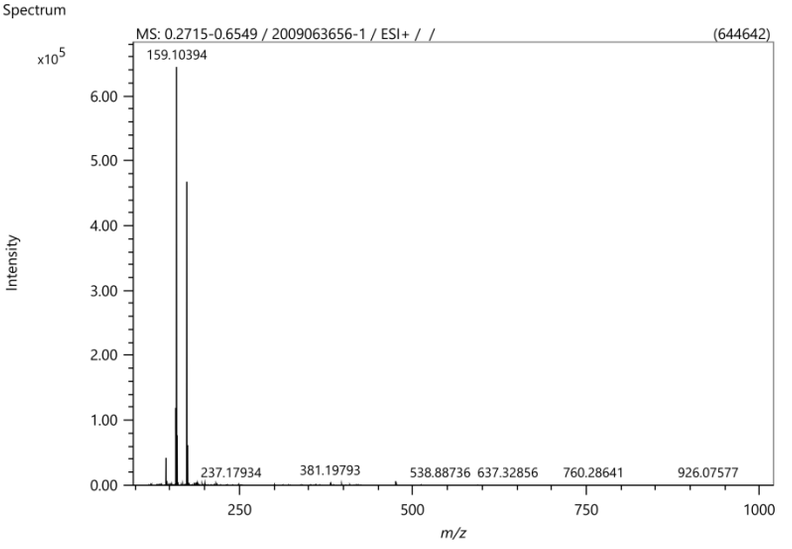

Elemental Composition

Parameters		Elements Set 1:							
Tolerance:	±5.00 ppm	Symbol	C	H	N	O	Na	S	Cl	Br
Electron:	Odd/Even	Min	0	0	0	0	0	0	0	0
Charge:	+1	Max	200	200	4	8	0	0	0	0
DBE:	-1.5 - 200.0									

Symbol	F	Si
Min	0	0
Max	0	0

Results

Mass	Intensity	Intensity [%]	Formula	Calculated Mass	Mass Difference [mDa]	Mass Difference [ppm]	DBE
174.12794	467889.18	72.58	C12 H16 N	174.12773	0.22	1.24	5.5

Figure S28. ^{1}H NMR (DMSO-d_6), HRMS of intermediate **A**.

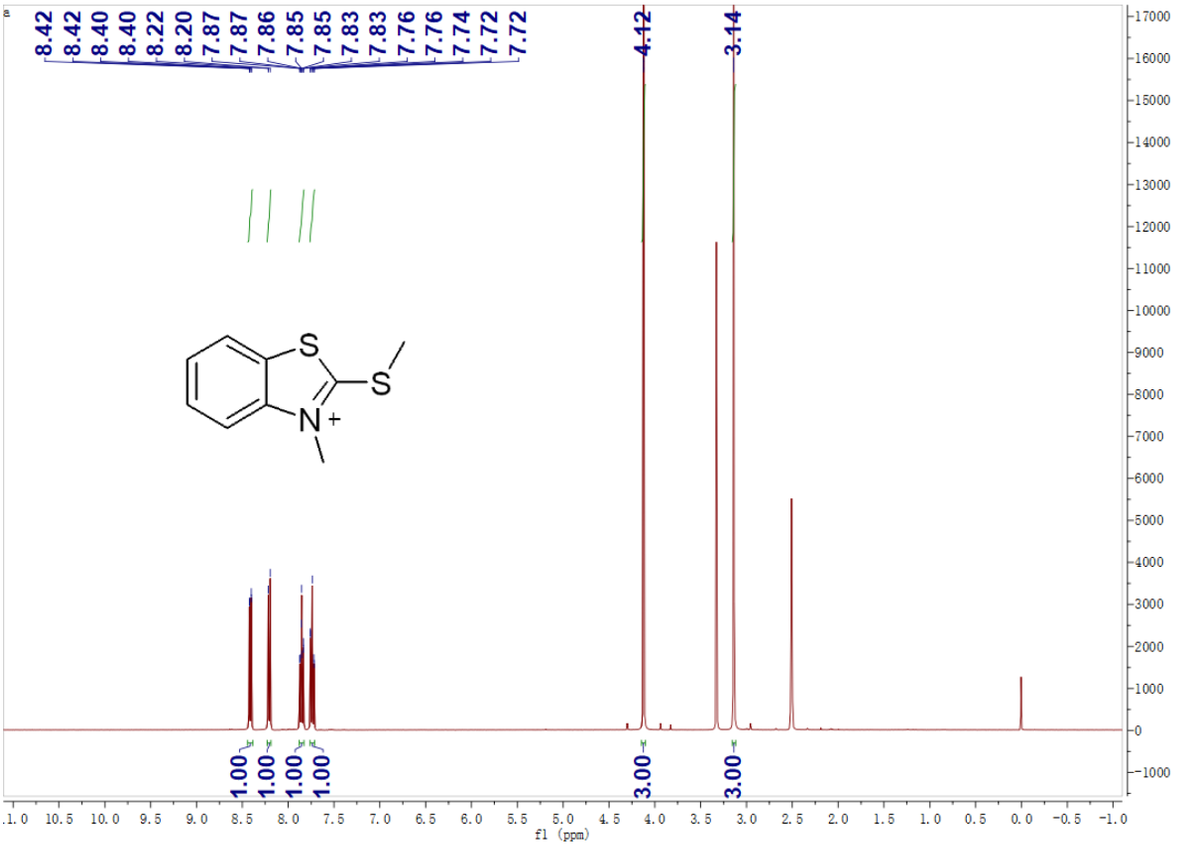

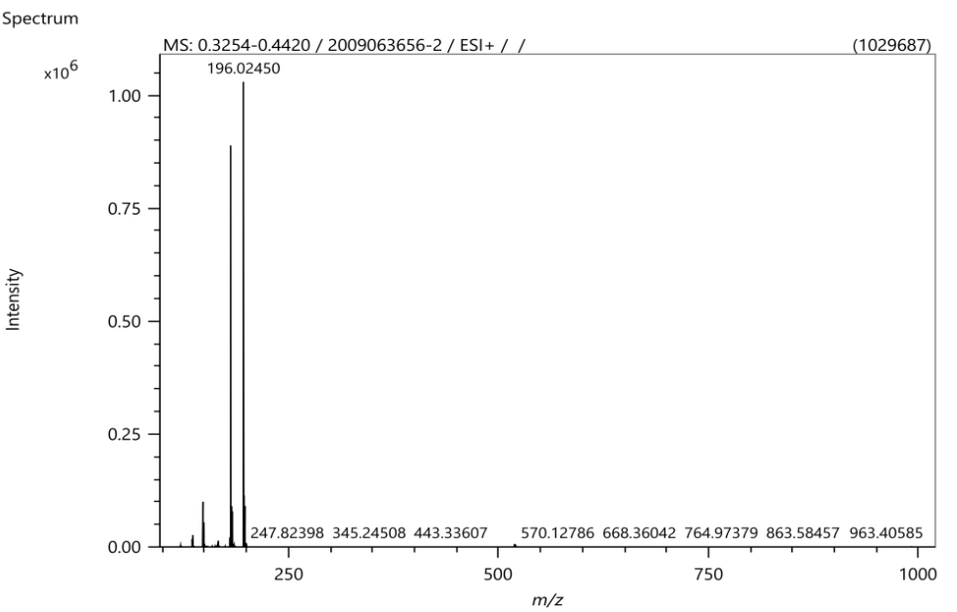

Elemental Composition

Parameters	
Tolerance:	±5.00 ppm
Electron:	Odd/Even
Charge:	+1
DBE:	-1.5 - 200.0

Elements Set 1:

Symbol	C	H	N	O	Na	S	Cl	Br
Min	0	0	0	0	0	2	0	0
Max	200	200	3	8	0	2	0	0

Symbol	F	Si
Min	0	0
Max	0	0

Results

Mass	Intensity	Intensity [%]	Formula	Calculated Mass	Mass Difference [mDa]	Mass Difference [ppm]	DBE
196.02450	1029686.71	100.00	C9 H10 N S2	196.02492	-0.41	-2.11	5.5

Figure S29. ^{1}H NMR (DMSO-d_6), HRMS of intermediate **B**.

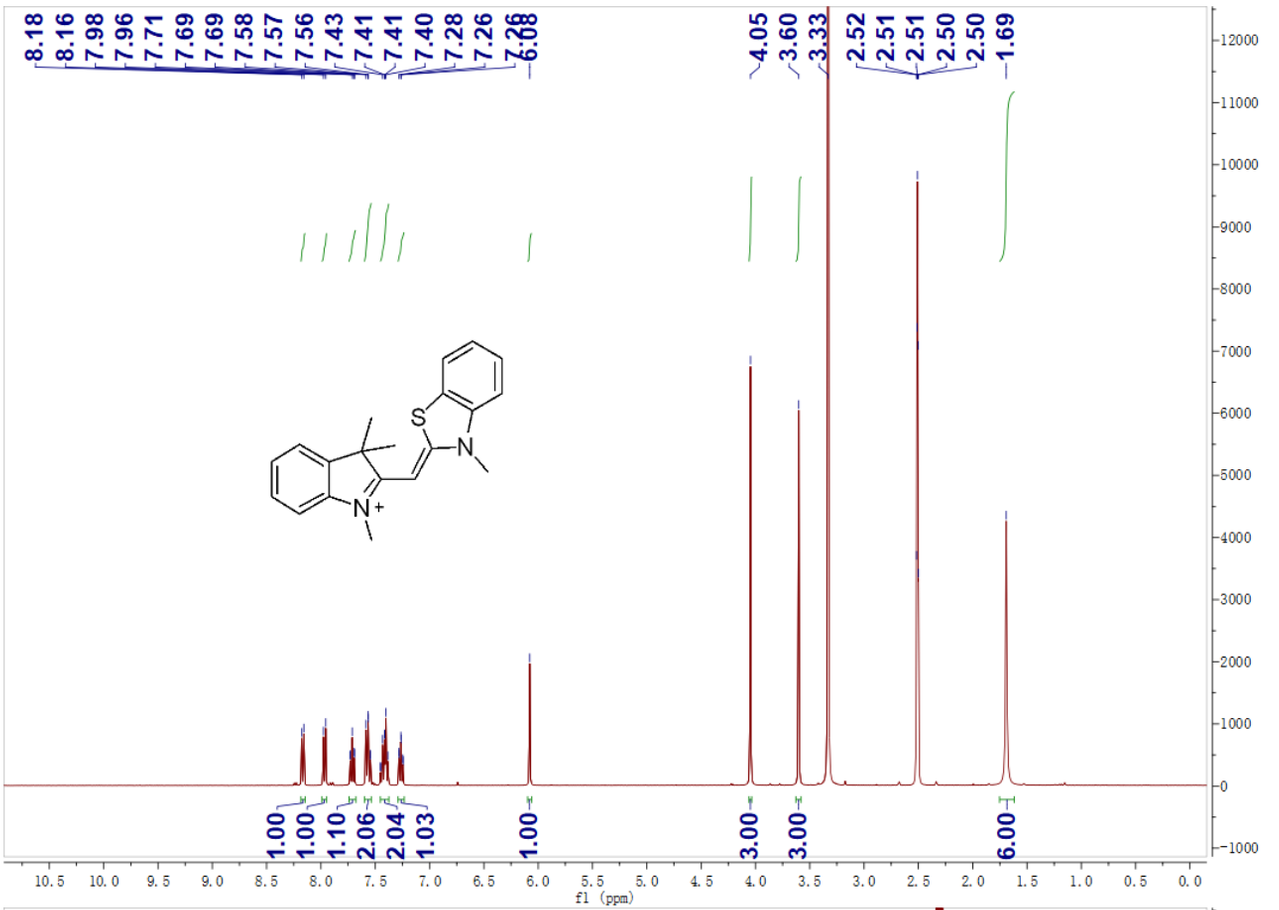
8.18
8.16
7.98
7.96
7.71
7.69
7.69
7.58
7.57
7.56
7.43
7.41
7.41
7.40
7.28
7.26
6.08
4.05
3.60
3.33
2.52
2.51
2.51
2.50
2.50
1.69
1.00
1.00
1.10
2.06
2.04
1.03
1.00
3.00
3.00
6.00
f1 (ppm)

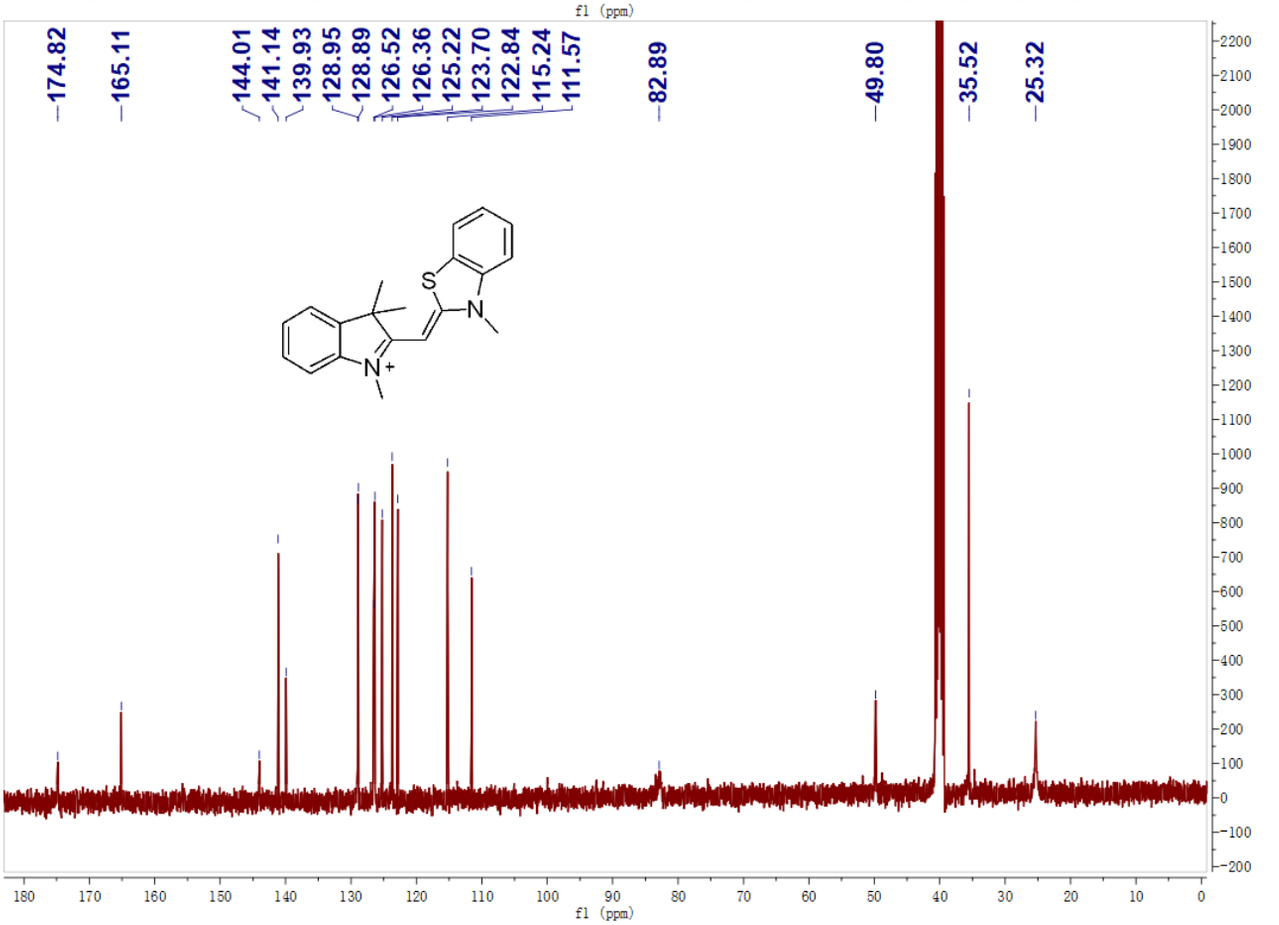
174.82
165.11
144.01
141.14
139.93
128.95
128.89
126.52
126.36
125.22
123.70
122.84
115.24
111.57
82.89
49.80
35.52
25.32
f1 (ppm)

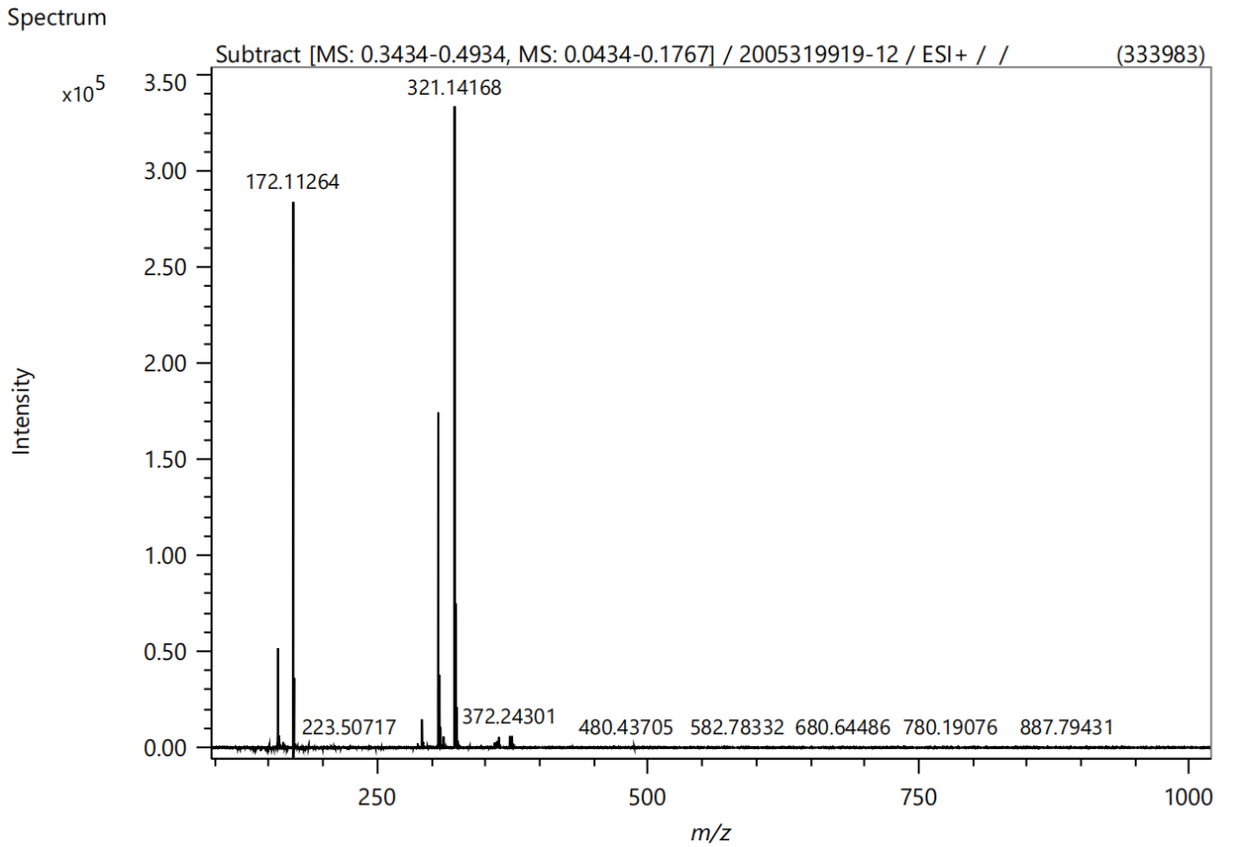

Elemental Composition

Parameters	
Tolerance:	±5.00 ppm
Electron:	Odd/Even
Charge:	+1
DBE:	-1.5 - 200.0

Elements Set 1:

Symbol	C	H	N	O	Na	S	Cl	Br
Min	0	0	0	0	0	1	0	0
Max	120	120	5	10	0	1	0	0

Symbol	F	Si	P	Mn	B	I	Ir
Min	0	0	0	0	0	0	0
Max	0	0	0	0	0	0	0

Results

Mass	Intensity	Intensity [%]	Formula	Calculated Mass	Mass Difference [mDa]	Mass Difference [ppm]	DBE
321.14168	333983.21	100.00	C20 H21 N2 S	321.14200	-0.31	-0.97	11.5

Figure S30. ^{1}H NMR (DMSO-d_6), ^{13}C NMR (DMSO-d_6), HRMS of **BZT-Indolium**.

Reference

1. G. M. Morris, R. Huey, W. Lindstrom, M. F. Sanner and A. J. Olson, *J. Comput. Chem.*, 2009, **30**, 2785–2791.
2. A. M. Brouwer, *Pure Appl. Chem.*, 2011, **83**, 2213–2228.
3. R. S. Tuma, M. P. Beaudet, X. Jin, L. J. Jones, C. Y. Cheung, S. Yue and V. L. Singer, *Anal. Biochem.*, 1999, **268**, 278-288.
4. T. Lemarteleur, D. Gomez, R. Paterski, E. Mandine, P. Mailliet and J. F. Riou, *Biochem. Bioph. Res. Co.*, 2004, **323**, 802-808.
5. W. Liu, C. Lin, G. Wu, J. Dai, T. C. Chang and D. Yang, *Nucleic Acids Res.*, 2019, **47**, 11931-11942.
6. S. Forli, R. Huey, M. E. Pique, M. F. Sanner, D. S. Goodsell and A. J. Olson, *Nat. Protoc.*, 2016, **11**, 905-919.